Research Paper

# Fully coupled hydro-mechanical–chemical continuum modeling of fluid percolation through rock salt

Ishmael Dominic Yevugah [a,b,*], Xiang-Zhao Kong [c], Antoine B. Jacquey [b], Christopher P. Green [d], Hartmut M. Holländer [a], Pooneh Maghoul [b,a]

[a] Department of Civil Engineering, University of Manitoba, Winnipeg, MB, Canada
[b] Department of Civil, Geological and Mining Engineering, Polytechnique Montréal, Montréal, QC, Canada
[c] Geothermal Energy and Geofluids Group, Department of Earth Sciences, ETH Zurich, Zurich, Switzerland
[d] CSIRO Energy, Clayton North, VIC, Australia

## ARTICLE INFO

## ABSTRACT

In domal and bedded rock salt geothermal reservoirs, geochemical dissolution of the in-situ rock salt formation can alter fluid transport properties, thus impacting fluid flow. Coupled Hydro-mechanical–chemical (HMC) modeling is a useful tool to evaluate fluid transport through rock salt geothermal systems and to assess their economic potential. Existing continuum-based numerical simulation of fluid transport through rock salt relies on the polyhedral orientation of rock salt crystal boundaries as potential fluid pathways, employing a deformation-dependent permeability model to depict pressure-driven fluid flow through rock salt. However, this numerical approach is exclusively HM-coupled and overlooks the influence of halite dissolution/precipitation on the permeability model. This study extends the deformation-dependent permeability model to account for halite dissolution by adopting a reverse mineral growth approach. Using this extended (HMC-coupled) model, we capture the relevance of geochemical reactions on the response of rock salt formations undergoing pressure-driven fluid percolation. The resulting simulations predict a lower fluid pressure than the HM-coupled scenario, highlighting the impact of halite dissolution on fluid flow through rock salt.

## 1. Introduction

Disposing of high-level radioactive waste or storing renewable energy resources in the subsurface requires the presence of a geologic formation used as a hydraulic barrier capable of withstanding potential hydraulic leaks or as a host for engineered caverns. Rock salt formations are often considered ideal hydraulic barriers because of their low porosity and permeability. In its undamaged state, rock salt is highly impermeable due to the extremely low porosity developed from exposure to high compaction rates throughout its geologic history.[1–3] The porosity of rock salt can be as low as 1%, or even 0.1% for bedded and domal salts.[4] Pure rock salt is an aggregate of polycrystalline evaporite grains,[5] which are impermeable and have no open boundaries except for thin boundary fluid layers.[4] Furthermore, rock salt generally lacks macroscopically interconnected pores, with only isolated pores possibly containing bulk fluid inclusions.[6] These characteristics render intact rock salt nearly impervious to fluid flow.

Recent laboratory experiments and field evidences unveiled several mechanisms that typically increase the porosity and permeability

of intact/undamaged rock salt, consequently promoting fluid influx. These permeability enhancement mechanisms can be shear-induced,[7,8] temperature-induced[3,9,10] or fluid pressure-induced.[2,9–13] As a result, these mechanisms undermine the hydraulic integrity of rock salt used as a hydraulic barrier.[2,4] They also offer valuable insights into the feasibility and economic potential of extracting geothermal fluids from domal and bedded rock salt formations.

Shear-induced failure occurs when an externally applied load induces a mechanical deviatoric stress on the rock salt formation. This mechanism leads to the formation of micro-cracks, which results in the dilatancy of the rock salt.[2,3,7,14] Dilatancy due to progressive damage leads to an increase in porosity and, hence, an increase in permeability. A common example of shear-induced failures is excavation of drifts and boreholes, which results in a so-called disturbed rock zone or excavated damage zone.[14]

Failures in rock salt can result from temperature variations associated with non-isothermal geo-environmental processes.[3] Such temperature fluctuations can generate tensile stresses that exceed the tensile

---

strength of rock salt, leading to the formation of micro-cracks that enhance in-situ permeability. This process, known as tensile fracturing, is often observed in underground energy storage reservoirs.[15] For instance, cyclic thermal loading and unloading from intermittent energy storage and extraction in salt caverns causes the rock salt to expand and contract, and often produce tensile cracks along the cavern walls.[3] Similarly, in salt caverns designated for radioactive waste disposal, heat generated from radioactive decay induces thermal stress, contributing to the development of tensile fractures along the cavern walls.

Fluid pressure can expand the grain boundaries of rock salt when it surpasses the in-situ stress and the rock salt tensile strength. Given the low tensile strength of rock salt (approximately $1\,\text{MPa}$[3]), fluid pressure often only needs to overcome the in-situ stress to open the grain boundaries.[4] The resulting openings facilitate fluid migration orthogonal to the minimum-acting stress (typically along preferential paths where grain boundaries experience the lowest normal stress).[2] This process is known as pressure-driven percolation (PDP)[11,16] or pressure-driven infiltration (PFI).[9,10,12,13] It is important to note that the preferential fluid pathways and the critical fluid pressure exceeding the normal stress are not intrinsic properties of the rock salt but are contingent on the in-situ stress state.[2]

Contrary to shear-induced dilatancy failures, which typically manifest within a few meters in the hydraulic barriers, PDP can extend across the entire hydraulic barrier, especially when subsidence of rock salt due to creep deformation and salt dissolution leads to stress redistribution. Therefore, PDP can result in significant fluid influx from adjacent porous hydrologic units, such as groundwater aquifers.[4]

Several other permeability enhancement mechanisms for rock salt are mentioned in the literature. For example, clay seams embedded within bedded salt formations may act as mechanical zones of weakness, thus promoting permeability and increasing fluid flow.[17] The presence of such heterogeneity can therefore negatively impact the integrity of rock salt as a geological barrier. Some authors also introduced the concept of a dihedral angle[18] — an angle formed between salt grains and liquid brine existing in textural equilibrium — and argued that it could be linked to the triggering of pore connectivity through a mechanism known as deformation-assisted percolation.[19] This phenomenon involves dynamic recrystallization of salt grains, and grain boundary wetting and stretching of brine inclusions into grain boundary films. However, recent experiments demonstrated that the dihedral angle holds no significant influence over the hydraulic integrity of rock salt.[2]

In addition to the geomechanical processes previously discussed, geochemical processes such as halite dissolution and precipitation can alter the phase composition of rock salt and compromise the hydraulic barrier integrity of its formations. Halite precipitation occurs when supersaturated brine permeates rock salt formations and evaporates due to in-situ temperature fluctuations.[20,21] In contrast, dissolution occurs when undersaturated fluids, such as freshwater, infiltrate these formations. These mechanisms can occur naturally when fluid from adjacent aquifers infiltrates the rock salt or due to imposed fluid pressure gradients by subsurface energy activities. Density-driven flows — arising from variations in temperature, salinity, or solute concentration — can further promote the infiltration of undersaturated fluids into rock salt. The resulting dissolution process can significantly undermine the hydraulic integrity of the rock salt formations.[22–24]

Given the intrinsic coupling complexity governing fluid flow in rock salt, numerical models are often used to quantify the impacts of geomechanical and geochemical processes on the fluid transport properties and the long-term hydraulic integrity of rock salt formations. A significant number of numerical models that simulate fluid transport through rock salt employs the discrete element method (DEM) due to its capability to capture the complex irregular flow pathways along the polycrystalline grains. However, DEM faces challenges in accurately computing conservation laws, and often requires long simulation times.[4] Hybrid codes, which combine DEM and continuum models,

address these challenges and are effective in predicting discontinuities at the grain scale.[25–28] Despite their accuracy at small scale, they are incapable of being applied effectively to large-scale modeling due to computational limitations.

To leverage the benefits of large-scale simulations and overcome the limitations of continuum models in replicating fluid flow pathways along the polycrystalline grain boundaries, Zill et al[4] proposed a permeability model within a continuum hydro-mechanical (HM) framework to describe pressure-driven percolation. This model extends the deformation-dependent permeability model proposed by Alonso et al.,[29] incorporating the nonlinear relationship between deformation-dependent permeability changes and fluid transport through rock salt.

In the pioneering model developed by Alonso et al[29] for gas transport through clay hydraulic barriers, parallel fracture sets were employed to simulate grain boundaries or potential flow paths within a continuous finite element framework. Rather than using an explicit joint element for these fracture sets, they assigned a homogenized intrinsic permeability property to the finite element domain. This homogenized intrinsic permeability property characterizes the fracture set in terms of fracture aperture, which, in turn, evolves in response to the material's deformation history.

In their extended model, Zill et al[4] departed from the concept of parallel fracture sets and considered potential fluid pathways in rock salt as a quasi-isotropic arrangement. They applied their model to simulate pressure-driven percolation through rock salt. Zill et al[4] showed that their HM model effectively replicated the results of hydrofrac experiments conducted on rock salt by Kamlot.[30] However, their model did not account for the impact of salt (or mineral) dissolution, a crucial geochemical process that can significantly alter the permeability of rock salt formations during subsurface energy storage or geothermal operations involving fluid injection into domal or bedded rock salt formations.

This study builds upon the deformation-dependent permeability model introduced by Zill et al[4] by incorporating salt dissolution reactions. We use a reverse application of the uniform mineral growth approach described by Grimm Lima et al.,[31] allowing the local (or rock salt) fracture apertures within the rock salt to increase in response to the dissolution of halite (NaCl) from the fracture surface. Unlike the simplified solubility-controlled equilibrium model presented by Grimm Lima et al.,[31] we implement a kinetic model for halite dissolution[32] based on the transition state theory (TST).[33] By integrating this dissolution-enhanced permeability model within the deformation-dependent permeability framework, we achieve more accurate predictions of the formation's overall absolute permeability.

As a case study, we use the benchmark experiment conducted by Kamlot[30] and its corresponding numerical simulation by Zill et al.[4] Specifically, we perform sensitivity analyses on the injected fluid, contrasting with the original experiment where spindle oil was used, which did not account for halite dissolution or precipitation. We address this research gap by substituting water as the injected fluid while maintaining the same stress magnitude, orientation, and boundary conditions as in the original hydro-frac experiment.

The main contribution of this work lies in assessing the behavior of rock salt undergoing pressure-driven percolation or infiltration, particularly focusing on the effect of halite dissolution, in its role as a hydraulic barrier of geothermal system. The model developed here could be further improved to address real environment issues in rock salt formations, such as subsidence, sinkhole formation, or total collapse due to halite dissolution caused by fluid infiltration.[34] In all these scenarios, the effect of in-situ geochemical reactions (e.g. halite dissolution) on the permeability of rock salt emerges as a critical parameter of interest.

Our fully coupled hydro-mechanical–chemical (HMC) simulation is single-phase with elastic constitutive mechanical behavior. The intricate simulations presented in this study are conducted using the MOOSE platform,[35] an open-source, parallel finite-element framework.

The rest of this paper consists of five sections, organized as follows. In Section 2, we discuss the equations underpinning our HMC model, encompassing conservation laws and constitutive behaviors, along with the requisite assumptions used in this study. In Section 3, we describe our extended permeability model. In Section 4, we conduct comprehensive case study simulations using our HM and HMC numerical codes, comparing the numerical results with the benchmark experiment of Kamlot[30] and the benchmark numerical simulations by Zill et al.[4] Finally, we discuss our findings in Section 5 followed by our conclusion.

## 2. HMC governing equations for single-phase flow through deformable porous media

In this section, we discuss the conservation laws in the context of the HMC behavior of rock salt when used as hydraulic barriers or geothermal systems. This includes the conservation of mass for the fluid phase, the conservation of momentum for the rock salt (porous) media, and the conservation of the amount (in moles) of the chemical species in our continuum (rock salt) model. We also describe the associated constitutive laws to close the set of conservation equations.

### 2.1. Model assumptions

The continuum rock salt model assumes a simple isotropic porous media undergoing transient Darcy flow with small deformations. Our simulation describes a single-phase fluid flow of multi-component reactive transport. The components include the injected fluid and the chemical species dissociated from the salt (halite) mineral. We maintain a constant temperature throughout, hence simulating isothermal conditions.

Rock salt displays a thermo-elastic-viscoplastic (TEVP) behavior with damage and healing when induced stresses exceed the dilatancy limit, as described by Hou.[14] Nonetheless, our model simplifies this behavior as an initial approximation, allowing us to assess its performance from a foundational perspective. This simplification assumes that the stresses induced by fluid pressure in the rock salt remain below its dilatancy limit and that viscoplastic deformation are negligible compared to the elastic one. These approximations are reasonable, given that the numerical scenarios we will consider in this study are at the laboratory scale with relatively low stresses (several MPa) and a finite execution time (less than a hour). We leave the exploration of higher induced stresses that exceed the dilatancy limit and over larger time scales for future work.

In our model, the Biot's coefficient $\alpha_B$ is set to a value of 1, chosen deliberately to ensure that the fluid pressure has maximum impact on the mechanical stress distribution. For a more practical value of $\alpha_B$, refer to (e.g. Ref. 36).

### 2.2. Fluid mass conservation and reactive transport

The governing equation controlling the single-phase but multi-component fluid flow through our deformable continuum porous media follows the notations introduced in Ref. 37 as follows:

$$\frac{\partial M^\kappa}{\partial t} + M^\kappa \nabla \cdot \boldsymbol{v}_s + \nabla \cdot \boldsymbol{F}^\kappa - \phi I^\kappa_{\text{chem}} - q^\kappa = 0, \tag{1}$$

where $M$ [kg m$^{-3}$] is either the fluid mass per unit volume (for conservation of fluid mass) or the solute mass concentration (for reactive transport), $\boldsymbol{v}_s = \frac{\partial \boldsymbol{u}}{\partial t}$ is the velocity [m s$^{-1}$] of the porous medium, $\boldsymbol{u}$ is the displacement, $t$ [s] is the time, $\boldsymbol{F}$ [kg s$^{-1}$ m$^{-2}$] is the fluid mass flux and $q$ [kg m$^{-3}$ s$^{-1}$] is the term for any external addition (source) or loss (sink) of mass. The superscript $\kappa$ indicates fluid components and primary solute species. In our study, the fluid component is H$_2$O, and the primary solute species are Na$^+$ and Cl$^-$. Finally, $\phi$ is the porosity of the porous media, and $I_{\text{chem}}$ [kg m$^{-3}$ s$^{-1}$] is the chemical dissolution/precipitation rate. In our study, $I_{\text{chem}} = I_m a_m M_s \rho_m$, where $I_m$ [mol m$^{-2}$ s$^{-1}$] is the kinetic rate of reaction (see Section 2.2.3), $M_s$

[kg mol$^{-1}$] is the molar mass of each chemical species, $\rho_m$ [kg m$^{-3}$] is the mineral density, and $a_m$ [m$^2$ kg$^{-1}$] is the mineral specific surface area for the reaction (see Section 3.1).

For fluid transport without chemical reaction (i.e., conservation of fluid mass only), Eq. (1) excludes the reaction term (i.e., $\phi I_{\text{chem}} = 0$). The source term, $q$, accounts for the fluid injection. Eq. (1) couples to deformation (or momentum balance equation) through the term $M^\kappa \nabla \cdot \boldsymbol{v}_s$. The coupling to the chemical reaction is fully implicit and appears through the reaction term in Eq. (1) (see Section 2.2.3 for further discussion). Therefore, our HMC model is fully coupled and fully implicit.

#### 2.2.1. Mass per unit volume

For single-phase flow, the fluid mass per unit volume in Eq. (1) follows[37]:

$$M^\kappa = \phi \rho_f \chi^\kappa_f. \tag{2}$$

Here, $\rho_f$ [kg m$^{-3}$] is the fluid density, and $\chi^\kappa_f$ [–] is the mass fraction of the $\kappa$-component in the fluid phase. The mass density equation requires that the total mass fraction of the fluid is unity, as shown in the following constitutive constraints below:

$$\sum_\kappa \chi^\kappa_f = 1. \tag{3}$$

#### 2.2.2. Mass flux

The mass flux, $\boldsymbol{F}^\kappa$, in Eq. (1) comprises an advective flux ($\boldsymbol{F}_{\text{adv}}$) and a diffusion-dispersive flux ($\boldsymbol{F}^\kappa_{\text{diffusion+dispersion}}$) for each component, as shown below[37]:

$$\boldsymbol{F}^\kappa = \chi^\kappa_f \boldsymbol{F}_{\text{adv}} + \boldsymbol{F}^\kappa_{\text{diffusion+dispersion}}. \tag{4}$$

The advective flux follows Darcy's law:

$$\boldsymbol{F}_{\text{adv}} = \rho_f \boldsymbol{v}_f = -\rho_f \frac{\boldsymbol{k}}{\mu_f} \left( \nabla P_f - \rho_f \boldsymbol{g} \right), \tag{5}$$

where $\boldsymbol{v}_f$ [m s$^{-1}$] is the Darcy fluid velocity, $\mu_f$ [Pa s] is the fluid dynamic viscosity, $P_f$ [Pa] is the fluid pressure, $\boldsymbol{g}$ [m s$^{-2}$] is the gravitational acceleration, and $\boldsymbol{k}$ [m$^2$] is the absolute permeability tensor, the crux of our model (see Section 3 for more discussion).

The diffusion and dispersive fluxes follow Fick's law:

$$\boldsymbol{F}^\kappa_{\text{diffusion+dispersion}} = -\rho_f \boldsymbol{D}^\kappa_f \nabla \chi^\kappa_f, \tag{6}$$

where $\boldsymbol{D}$ [m$^2$ s$^{-1}$] is the hydrodynamic dispersion tensor as follows:

$$\boldsymbol{D}^\kappa_f = D^\kappa_T \boldsymbol{I} + \left( D^\kappa_L - D^\kappa_T \right) \frac{\boldsymbol{v}_f \boldsymbol{v}_f}{\|\boldsymbol{v}_f\|^2}, \tag{7}$$

with $\boldsymbol{I}$ being the unit matrix and the longitudinal ($D^\kappa_L$) and transverse ($D^\kappa_T$) dispersion coefficients of each component given as:

$$D^\kappa_L = d^\kappa_f + \alpha_L \|\boldsymbol{v}_f\|, \quad \text{and} \quad D^\kappa_T = d^\kappa_f + \alpha_T \|\boldsymbol{v}_f\|, \tag{8}$$

and $d^\kappa_f$ [m$^2$ s$^{-1}$] is the molecular diffusion coefficient for each component (we take $1 \times 10^{-9}$ m$^2$ s$^{-1}$[38]) and $\|\boldsymbol{v}_f\|$ [m s$^{-1}$] is the magnitude of the Darcy velocity flux. The longitudinal ($\alpha_L$ [m]) and transverse ($\alpha_T$ [m]) dispersivities are $1 \times 10^{-2}$ m and $1 \times 10^{-3}$ m[39] respectively, considering the laboratory scale of our simulation.

#### 2.2.3. Geochemical kinetic reactions

Geochemical reactions occur when the existing in-situ chemical equilibrium in rock salt formations is destabilized due to the injection of "fresh" fluids (i.e. unsaturated with salt), thus altering the transport properties of the rock salt formation. Typically, the transport of chemical species is assisted with a source or sink term of species mass, which provides a means to ensure mass balance among minerals and the dissolved species,[40–43] as shown in the chemical precipitation/dissolution term ($\phi I_f$) in Eq. (1).

In this study, we simulate the injection of freshwater by setting the concentrations of primary chemical species (i.e., $Na^+$ and $Cl^-$) in the injected fluid to zero. In our current configurations, supersaturation of halite is unfavorable, and its precipitted is considered negligible. A practical application of this model is in the context of rock salt geothermal energy systems, where continuous injection of undersaturated fluid during the heat exchange process can lead to significant dissolution.

The dissolution of halite follows the following chemical equilibrium equation[44]:

$$NaCl_{(s)} \leftrightharpoons Na^+_{(aq)} + Cl^-_{(aq)}, \tag{9}$$

where $NaCl_{(s)}$ is the halite mineral (solid phase), $Na^+_{(aq)}$ and $Cl^-_{(aq)}$ are the dissolved chemical species in the dissolution reaction.

This study follows the transition state theory (TST),[33] and specifically uses the rate law presented by Seales et al[32] to quantify the dissolution or detachment of the primary species from the halite surface. TST dictates that a mineral reacts (e.g., dissolves or precipitates) by creating an activated complex (a reaction's transition state). This activated complex characterizes the potential energy threshold needed for the reaction.[32] The rate at which the activated complex decays quantifies the reaction rate.[45] Specifically for mineral dissolution, desorption kinetics controls the decay rate of the activated complex formed on the surface of the dissolving mineral.[32]

Mathematically, the halite dissolution rate used in this study takes the following form[46]:

$$I_m = \frac{dm_{Na^+}}{dt} = \frac{dm_{Cl^-}}{dt} = r_+ \left[ 1 - \exp\left( -\frac{A_c}{\sigma_s RT} \right) \right], \tag{10}$$

where $\frac{dm_i}{dt}$ [mol m$^{-2}$ s$^{-1}$] is the mass flux of primary species across a unit surface area of the rock salt, and $r_+$ [mol m$^{-2}$ s$^{-1}$] presents the intrinsic dissolution rate constant of halite in an infinitely dilute solution, $R$ [8.3143 J K$^{-1}$ mol$^{-1}$] is the gas constant, $T$ [K] is the absolute temperature, $A_c$ [J mol$^{-1}$] is the chemical affinity of the reaction, and $\sigma_s$ is Temkin's average stoichiometric number, a parameter used to fit the dissolution rate to experimentally obtained values.[44] In this study, we used $\sigma_s = 2$.[32] The intrinsic rate constant ($r_+$) in Eq. (10) is a function of the in-situ absolute temperature via the Arrhenius phenomenological law, shown as[47]:

$$r_+ = A_f \exp\left( -\frac{E_A}{RT} \right), \tag{11}$$

where $A_f$ [mol m$^{-2}$ s$^{-1}$] is the Arrhenius pre-exponential factor, and $E_A$ [J mol$^{-1}$] is the activation energy. Note that the activation energy and the pre-exponential factor are fitted parameters determined empirically by measuring the intrinsic rate at various absolute temperatures. The intrinsic rate of $r_+$ for halite dissolution is measured to be 0.806 354 mol m$^{-2}$ s$^{-1}$ at an absolute temperature of 327.59 K.[32]

The chemical affinity defines the reaction's thermodynamic equilibrium state as follows,[32] $A_c = -RT \ln(Q/K_{eq})$. The substitution of the chemical affinity into Eq. (10) leads to:

$$I_m = r_+ \left[ 1 - (Q/K_{eq})^{1/\sigma_s} \right]. \tag{12}$$

Here, $K_{eq}$ [mol$^2$ kg$^{-2}$] is the thermodynamic equilibrium constant for the halite dissolution reaction, and $Q$ [mol$^2$ kg$^{-2}$] is the dissolution ionic activity product for activities of $Na^+$ and $Cl^-$ (i.e., $a_{Na^+}$ and $a_{Cl^-}$). Note that the chemical affinity determines the thermodynamic drive of the reaction based on the $Q/K_{eq}$ term. Dissolution only occurs when the fluid is undersaturated (i.e., $Q < K_{eq}$) with halite. Otherwise, precipitation occurs due to supersaturation ($Q > K_{eq}$) of the fluid with halite.[45]

In an aqueous solution, ions of chemical species are less concentrated than their true experimentally measured concentrations due to inter-ionic electrostatic interaction and their interaction with $H_2O$ molecules. This effective concentration is the species' activity ($a_s$). The activity of a species relates to its concentration (species molality $C_s$ [mol kg$^{-1}$ (of $H_2O$)]) through an activity coefficient ($\gamma_s$) as follows:

$$a_s = \gamma_s C_s. \tag{13}$$

Here the concentration ($C_s$) is computed as $C_s = \chi^s_f / (\chi^{H_2O}_f \cdot M_s)$, where $\chi^s_f$ is the solute mass fraction in Eq. (2), the superscript $s$ stands for $Na^+_{(aq)}$ and $Cl^-_{(aq)}$, and $M_s$ [kg mol$^{-1}$] is the molar mass of individual chemical species ($M_{Na} = 23$ g mol$^{-1}$ and $M_{Cl} = 35.45$ g mol$^{-1}$).

Different formulations, such as the Debye–Huckel and Virial Methods (and their variations), exist for computing the activity coefficients based on the ionic strength of the aqueous solution.[32,45] For surface and groundwater numerical simulations, the Extended Debye–Huckel model and Guntelberg approximations are most efficient up to ionic strengths below 0.1 molal, and the Davies equation is efficient below 0.5 molal.[32] The most preferred, however, is the Debye–Huckel B-dot model because it is suitable for solutions with temperatures of 0 °C to 300 °C, and is considered reasonably accurate for predicting the activities of $Na^+$ and $Cl^-$.[45] However, the Debye–Huckel B-dot model is shown to be inefficient beyond the ionic strength of 3 molal. To overcome this drawback and considering the expected high concentration of $Na^+$ and $Cl^-$ in the aqueous solution of our study, we implement the modified Pitzer's specific ion interaction (SII) model.[32] The Pitzer's SII model works for an ionic strength up to 20 molal, and its activity coefficient takes the following form[48,49]:

$$\log \gamma_i = -\frac{A z_i^2 \sqrt{I}}{1 + \mathring{a}_i B \sqrt{I}} - \sum_j B_{ij} C_j, \tag{14}$$

$$\log \gamma_j = -\frac{A z_j^2 \sqrt{I}}{1 + \mathring{a}_i B \sqrt{I}} - \sum_i B_{ij} C_i, \tag{15}$$

where $\gamma_i$ and $\gamma_j$ define the activity coefficients for the cation ($i$) of molality $C_i$ and anion ($j$) of molality $C_j$, respectively, $z_s$ and $\mathring{a}_s$ [Angstrom, Å] are the corresponding ionic charge and (ionic) size parameters available in any reliable geochemical database employed for geochemical simulations (for example, GeochemistWorkBench (GWB)[50] and EQ3/6[51]). We perform our simulations with MOOSE which uses parameters from the GWB thermodynamic database.

Parameters $A$ [mol$^{-1/2}$ kg$^{1/2}$] and $B$ [mol$^{-1/2}$ kg$^{1/2}$ Å$^{-1}$] for the SII model vary with temperatures and pressures, and are defined as[32,52]:

$$A \equiv \frac{(2\pi N)^{1/2}}{2.302585 (1000)^{1/2}} \frac{e^3 \rho_m^{1/2}}{(\varepsilon KT)^{3/2}} = \frac{1.824 482 923 8 \times 10^6 \rho_m^{1/2}}{(\varepsilon T)^{3/2}}, \tag{16}$$

$$B \equiv \left( \frac{8\pi N \rho_m e^2}{1000 \varepsilon KT} \right)^{1/2} = \frac{50.291 586 49 \times 10^8 \rho_m^{1/2}}{(\varepsilon T)^{1/2}}. \tag{17}$$

Here $N$ [6.022 52 × 10$^{23}$ mol$^{-1}$] is Avogadro's number, $e$ [1.602 176 634 × 10$^{-19}$ C] is the absolute electronic charge and $\varepsilon$ is the dielectric constant of $H_2O$.[53] $T$ [K] is the in-situ temperature of our system, and $K$ [1.380 649 × 10$^{-23}$ J K$^{-1}$] is the Boltzmann's constant. The binary specific ionic interaction coefficient ($B_{ij}$ [kg mol$^{-1}$]) in Eqs. (14) and (15) depends on (and varies with) the ionic strength of the concentrated aqueous solution[32,49]:

$$B_{ij} = B_{ij}^\infty + (B_{ij}^0 - B_{ij}^\infty) \cdot F(I). \tag{18}$$

Here $B_{ij}^0$ [0.159 kg mol$^{-1}$] and $B_{ij}^\infty$ [0.0486 kg mol$^{-1}$][49] are constant values of $B_{ij}$ at zero and infinity ionic strengths, respectively. The empirical function, $F(I)$, depends on the ionic strength ($I$ [mol kg$^{-1}$]).[32] The ionic strength of the aqueous solution is a function of the concentration of all ions present in the solution, as shown below:

$$I = \frac{1}{2} \sum_s z_s^2 C_s. \tag{19}$$

### 2.3. Geomechanics

For a porous medium under static mechanical equilibrium, the conservation of momentum is the divergence of the Cauchy total stress tensor ($\sigma_{ij}$ [Pa]), written in terms of Biot's effective stress tensor ($\sigma'_{ij}$ [Pa]), as follows:

$$\nabla \cdot \left( \sigma'_{ij} - \alpha_B P_f \delta_{ij} \right) = 0, \tag{20}$$

where $\alpha_B$ is Biot's coefficient, typically ranging from 0 to 1 (taken as 1 in this study. See Section 2.1). $P_f$ [Pa] is the fluid pressure, and $\delta_{ij}$ is the Kronecker delta. Our formulations consider material engineering convention, where the stress is negative in compression. The Cauchy total stress tensor is given as[54–56]:

$$\sigma_{ij} = \sigma'_{ij} - \alpha_B P_f \delta_{ij}. \tag{21}$$

Assuming the porous medium is linearly elastic, a constitutive relationship exists between Biot's effective stress and the generated elastic strain tensor ($\varepsilon^e_{kl}$) through Hooke's law as follows:

$$\sigma'_{ij} = E_{ijkl} \varepsilon^e_{kl}, \tag{22}$$

where $E_{ijkl}$ [Pa] is the fourth-order elasticity tensor. For a symmetric isotropically elastic material, $E_{ijkl} = \left( K - \frac{2}{3} G \right) \delta_{ij} \delta_{kl} + G(\delta_{ik} + \delta_{jl})$ expressed with the shear modulus ($G$ [Pa]) (also called the second lame's parameter) of the porous media and the bulk modulus ($K$ [Pa]) results in:

$$\sigma'_{ij} = 2G\varepsilon^D_{ij} + K \varepsilon^e_{kk} \delta_{ij}, \tag{23}$$

where $\varepsilon^D_{ij}$ is the deviatoric strain tensor and $\varepsilon^e_{kk}$ is the volumetric strain tensor or trace of the elastic strain tensor. The total strain tensor is calculated with the small strain approximation as follows:

$$\varepsilon^e_{ij} = \frac{1}{2} \left( u_{i,j} + u_{j,i} \right), \tag{24}$$

where $u$ [m] is the displacement vector of the porous medium. The small strain tensor assumes that (for small deformations considered here) the second-order terms in the deformation gradient are negligible.

Rock salt creeps with time (i.e., shows time-dependent or viscoplastic strain[57]) during a long period of constant applied external load. Furthermore, when the external load exceeds the dilatancy limit of the rock salt, it can induce damage within the rock salt. The damage may further accelerate[57] or heal by crack closure and re-bonding[58] when the applied stresses relax. Various models have been proposed to account for this inelastic strain for rock salt (see[4] for a summary) including the modified Lubby2 model.[59,60] In this study, we only consider scenarios at the laboratory scale with low induced stresses applied over a limited time. Under these conditions, the first-order deformation mechanism of rock salt is elastic and time-dependent deformation is negligible. For this reason, we consider the rock salt to deform elastically in this study.

## 3. Permeability evolution

As our HMC model considers the effect of pressure-driven percolation, we extended the permeability model developed by Zill et al[4]. Their permeability model efficiently captured the preferential flow of fluid through rock salt. However, their model does not incorporate the effect of salt dissolution. By leveraging the reaction/dissolution model discussed in Section 2.2.3, we include the effect of halite dissolution in their permeability model, based on a reverse mineral growth approach. This approach is the antithesis of the uniform mineral growth approach intended for salt precipitation.[31] We briefly review the current permeability model here with a detailed discussion of our extension.

The original permeability model proposed by Alonso et al[29] is a homogenized representation of a set of parallel micro-fractures. These parallel fracture sets indicate grain boundaries (so-called micro-fractures or potential flow paths) in a continuous finite element rock salt volume

(see Fig. 1). Instead of explicitly representing these parallel fracture sets as a lower dimensional element in each finite element of a discretized continuum model, the permeability formulation implicitly captures the geometry of the fracture sets in terms of the fracture aperture ($b$ [m]), mean fracture spacing ($a$ [m]) and a unit vector orthogonal to the fracture ($\hat{n}$). Consequently, the mathematical solution to the permeability model at each finite element node inherently comprises these parallel fracture sets without physically representing them.

Conceptually, the absolute permeability tensor ($k$ [m²]) of the model is a combination of the intrinsic permeability parallel to the fracture plane ($k_\parallel$ [m²]) and that perpendicular to the fracture plane ($k_\perp$ [m²]), as shown below:

$$k = k_\perp M + k_\parallel (I - M), \tag{25}$$

in which $M = \hat{n} \otimes \hat{n}$ is a structure tensor used to weight the two components, $k_\perp$ and $k_\parallel$. Typically, $k_\perp$ is the matrix permeability ($k_m$ [m²]), and $k_\parallel$ is the weighted average of the matrix permeability and fracture permeability ($k_f$ [m²]). The weights are based on their corresponding volume fractions, as follows:

$$k_\parallel = \left( \frac{s - nb}{s} k_m + \frac{nb}{s} k_f \right), \tag{26}$$

where $s$ is the height of the finite element along the direction of $\hat{n}$, and $n$ is the number of fractures in this finite element volume, as shown in Fig. 1.

Substitution of Eq. (26) into Eq. (25) yields:

$$k = k_m M + \left( \frac{s - nb}{s} k_m + \frac{nb}{s} k_f \right) (I - M), \tag{27}$$

and further

$$k = k_m I + \frac{nb}{s} \left( k_f - k_m \right) (I - M). \tag{28}$$

By introducing the fracture permeability using the cubic law, $k_f = b^2/12$, Ref. 61 through the parallel plate approximation, and considering that the height of the finite element is the product of the number of fractures ($n$) present in the finite element volume and the mean fracture distance ($a$). A further simplification of Eq. (28) gives:

$$k = k_m I + \frac{b}{a} \left( \frac{b^2}{12} - k_m \right) (I - M). \tag{29}$$

The crux of this permeability model is the rock salt grain boundaries (or the micro-fracture apertures) characterizing the preferential flow paths in the rock salt. Because the matrix permeability of rock salt is extremely low, this permeability model assumes that fluid only flows through rock salt if variations in strain due to injected fluid overcome existing grain boundaries (or the micro-fracture apertures) in the rock salt. Therefore, the model comprises an initial micro-fracture aperture with a minimum permeability value ($b_0 = \sqrt{12 k_m}$ [m]), and a strain-dependent fracture aperture ($\Delta b$ [m]). This minimum initial micro-fracture (or grain boundary) permeability is over 100 times the matrix permeability (i.e., $b_0 = \sqrt{12 \times 10^{-21}}$ [m]), considering that the matrix permeability of rock salt is typically $1 \times 10^{-21}$ m².[4] Consequently, matrix permeability is constant in the rock salt, thus allowing fluid flow through only the grain boundaries. The strain-dependent fracture aperture varies with the strain orthogonal to the fracture plane (i.e., the fracture-normal strain, $\varepsilon_n$). This mutual dependence between the micro-fracture aperture and the orthogonal strain occurring in the model ensures that the grain boundaries or the preferential flow paths open, as shown mathematically below:

$$b = b_0 + \Delta b, \tag{30}$$

$$\Delta b = a \langle \varepsilon_n - \varepsilon_0 \rangle. \tag{31}$$

Here, the terms in the Macaulay brackets, $\langle x \rangle$, physically means that the change in fracture aperture only increases and cannot be negative. The initial/threshold strain state of the material, $\varepsilon_0$, must
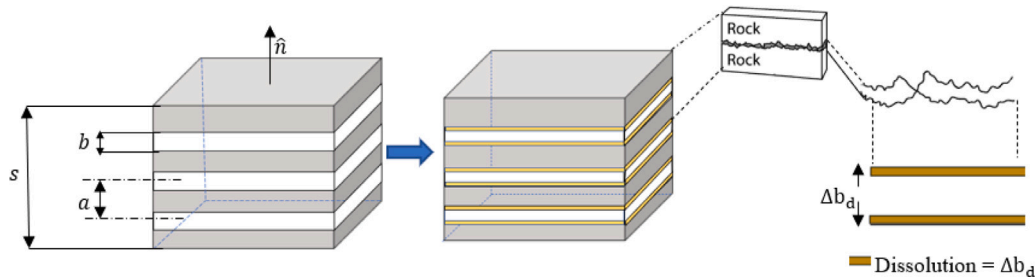
**Fig. 1.** From left to right: (1) Conceptual volume element of rock salt with the embedded parallel fracture set; (2) Conceptual model of the same fracture set after dissolution processes; (3) Schematic representation of actual fracture with rough walls; (4) Schematic of a rough-walled fracture and its conceptual model for fracture aperture change due to salt dissolution.

always be smaller than $\varepsilon_n$ for aperture change to occur (i.e., $\varepsilon_n > \varepsilon_0$). Negative values of $\varepsilon_0$ denote closed fracture apertures at only certain compressive strains but not close at zero strain.[4]

Further extension of this permeability model to rock salt (and any polycrystalline media, for that matter) accounts for the fact that rock salt has a polyhedral orientation of crystal boundaries that act as potential fluid flow pathways if activated by deformation.[4] Therefore, instead of parallel fracture sets, the permeability model assumes a homogenized representation of three orthogonal embedded crystal boundaries at each finite element. The orientation of these triplet crystal boundaries varies spatially to form a quasi-isotropic or quasi-random orientation of the preferential flow paths. Therefore, the permeability model assumes a summation of three independent orthogonal fracture planes as follows:

$$k = k_m I + \sum_{i=1}^{3} \frac{b_i}{a_i} \left( \frac{b_i^2}{12} - k_m \right) (I - M), \tag{32}$$

where the fracture aperture of the $i$-component of the triplet orthotropic crystal boundary at a finite element can be formulated as follows:

$$b_i = b_{i0} + a_i \langle \varepsilon_n : M_i - \varepsilon_{0i} \rangle. \tag{33}$$

A unique attribute of this orthotropically embedded fracture permeability model is that it can simulate an anisotropic permeability of a certain magnitude and direction, depending on the in situ stress field and the induced deformation in response to coupled or separate hydraulic and mechanical loadings without specifying *a priori* anisotropy.[4] In the following, we introduce the effect of mineral dissolution on the permeability model.

### 3.1. Extension of both the parallel and orthotropically embedded fracture permeability model to account for mineral dissolution

In alignment with Grimm Lima et al.,[31] this study introduces an extension to the existing permeability models, specifically the parallel model[29] and the orthotropically embedded fracture model.[4] Our proposal expands these models by incorporating the recognition that changes in fracture aperture, as modeled by these permeability frameworks, can result not only from variations in strain but also from dynamic geochemical reactions. Therefore, we further assumed that the rock salt is initially at chemical equilibrium with its thin grain boundary layer fluid (water). An injection of "fresh" unsaturated fluid mainly goes through only the grain boundaries, causing halite dissolution and modifying the grain boundaries (or the micro-fracture aperture). We characterized the dissolution of the rock salt using the halite kinetic rate law. However, extending the proposed permeability model to encompass other rock formations beyond rock salt is achievable by incorporating a suitable geochemical reaction kinetic rate law.

We adopt a uniform modification approach for fracture aperture evolution within a computation grid, as outlined by Grimm Lima et

al.[31] This method adjusts the fracture aperture according to the dissolution volume of NaCl mineral on fracture surfaces, which in turn influences the overall absolute permeability (see Fig. 1).

The kinetic rate of halite dissolution here follows the one from Ref. 32 (see Section 2.2.3). Considering both the strain and dissolution alternation on fracture aperture, the fracture aperture ($b$ [m]) in the parallel embedded fracture permeability model can be formulated as follows:

$$b = b_0 + a \langle \varepsilon_n - \varepsilon_0 \rangle + \Delta b_d, \tag{34}$$

where $\Delta t$ [s] is the time step size, and $\Delta b_d$ [m] is the change in fracture aperture due to dissolution.

Our permeability model assumes that the fracture aperture evolves uniformly and progressively by the removal of a thin layer of thickness given by $\Delta b_d/2$ (Fig. 1) on both sides of the fracture surface. This assumption yields an increase of fracture volume at any point/node equivalent to the total dissolved mineral volume at that node/point ($\Delta V_{m,d}$ [m$^3$]),

$$\Delta b_d = \frac{\Delta V_{m,d}}{A_{b,p}} \tag{35}$$

where $A_{b,p}$ [m$^2$] is the total fracture surface area at a given point/node. Considering the conceptual model of parallel fracture set, the total fracture surface can be computed as $A_{b,p} = 2 V_p/a$ (Fig. 1), where $V_p$ [m$^3$] is the element volume at a given point/node. This conceptual model yields a specific surface area of the fractured rock salt, $a_m = A_{b,p}/(V_p \phi \rho_m) = 2/(a \phi \rho_m)$. The total dissolved mineral volume ($\Delta V_{m,d}$) can be computed as $\Delta V_{m,d} = I_m M_{\text{halite}} A_{b,p} \Delta t/\rho_m$, where $\rho_m$ [kg m$^{-3}$] is the mineral density (for halite in this case) and $M_{\text{halite}} = 58.45\,\text{g mol}^{-1}$ is the molar mass of halite. Substitution of these relationships into Eq. (35) yields the rate of change in fracture aperture

$$b_d = \frac{\Delta b_d}{\Delta t} = \frac{I_m M_{\text{halite}}}{\rho_m} \quad . \tag{36}$$

The fracture aperture for the ortho-tropically embedded permeability model can be updated as follows:

$$b_i = b_{i0} + a_i \langle \varepsilon_n : M_i - \varepsilon_{0i} \rangle + \Delta b_{id}, \tag{37}$$

where $\Delta b_{id}$ [m] is the change in fracture aperture for the $i$-component of the triplet orthotropically oriented crystal boundary.

Substituting of the updated fracture aperture in Eq. (37) into equation (32) yields our novel permeability model, which accounts for both mechanical and geochemical effects (HMC coupled) on permeability evolution of rock salt. It is worth noting that in Eq. (32), the only variable parameter is the updated micro-fracture aperture (or the grain boundary). All other parameters remain constant, following the earlier assumption that the matrix permeability is extremely low and, hence, remains unaffected by fluid flow or reactive transport process.

In our HM and HMC models, the permeability model (Eq. (32)) updates the permeability using a linear iteration procedure based on our proposed fracture aperture change (see Fig. 2). The process begins at the first time-step, where apertures of the original orthotropic
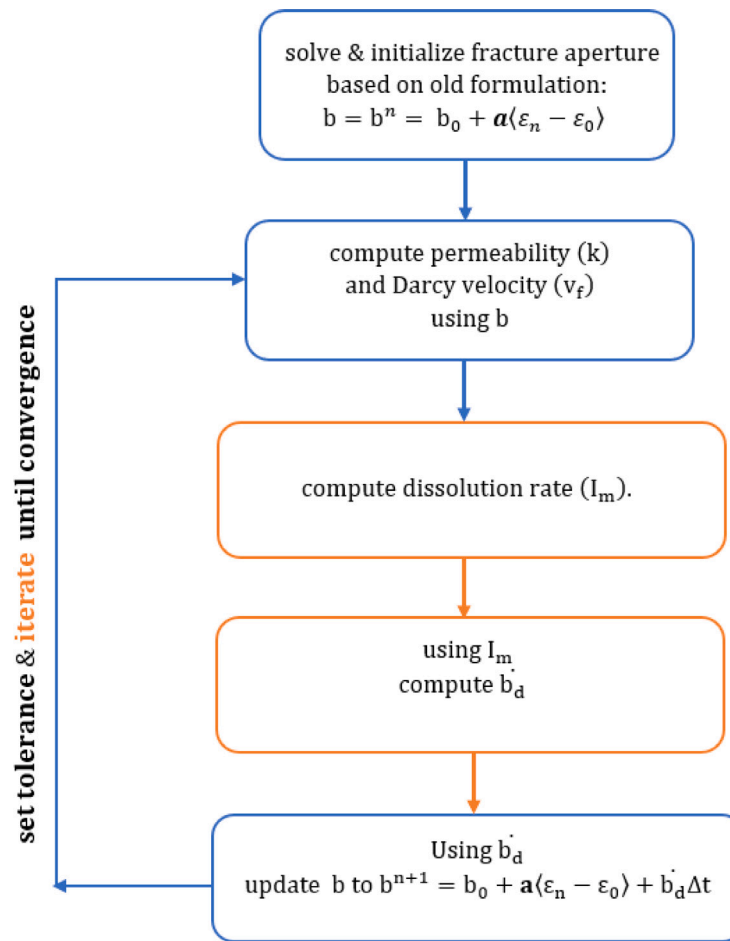
**Fig. 2.** Permeability iteration algorithm based on fracture aperture alteration with time due to halite dissolution.
*Source:* Adapted from Ref. [31].

fractures are computed and initialized (Eq. (33)). Using this initial fracture aperture, the permeability and the Darcy's velocity are calculated (Eq. (5)) after the governing equation (Eq. (1)) is resolved. The primary species concentrations are then computed with the governing equation (1) and the dissolution reactions (Eq. (12)). The fracture apertures are then updated according to out HMC model (Eq. (37)). The updated fracture aperture serves as an input for recalculating the permeability and the reactive transport process in the subsequent time-step. This iterative cycle continues until the solution converges within a specified tolerance.

We recognize that the assumption of uniform dissolution along the fracture surfaces is a simplification, given the complex and heterogeneous nature of dissolution processes that can occur along the fracture aperture walls.[31] Nevertheless, this approach serves as a foundational step to evaluate the new permeability model. Using this dissolution-dependent fracture aperture evolution technique, our proposed permeability model effectively incorporates the impact of geochemical reactions on the transport phenomenon in fractured porous media based on the pressure-driven percolation theory.

## 4. Numerical simulations and results

This section describes a series of simulations, with a particular focus on the hydro-frac experiment conducted by Kamlot,[30] which serves as a case study. For the verification of the halite geochemical reaction component (pure dissolution) of the proposed HMC model, refer to Appendix. In all our simulations, the $Na^+$ and $Cl^-$ concentrations are equivalent and expressed in $mol\,kg^{-1}$ of water (see Eq. (9)).

### 4.1. Verification of our new permeability model against a benchmark simulation

To evaluate the validity and applicability of our novel permeability model, we perform simulations against the numerical benchmark conducted by Zill et al.,[4] which is based on experimental observations by Knauth.[62] In this verification, we used water as the working fluid. The verification setup involves injecting fluid into a hydrostatically stressed cylindrical volume of a rock through a borehole.

Because of the symmetry of the experiment, the simulation considers only a 2D quadrant of the cylindrical rock sample. This quadrant has a radius of $10\,m$, with an inner borehole radius of $2\,m$ shown in Fig. 3. Fluid is injected through the borehole at a constant pressure of $P_{hole} = 1\,MPa$, and a compressive stress of the same magnitude ($\sigma_{hole} = 1\,MPa$) is applied to the borehole wall. The outer boundary of the 2D quadrant is set to a fluid pressure ($P_{edge}$) and stress ($\sigma_{edge}$) both at 0.1 MPa. The initial halite concentration of the rock salt is $1\,mol\,kg^{-1}$. Our simulation is conducted under isothermal conditions with a temperature of 327.594 K. "Fresh" water with a halite concentration of $0\,mol\,kg^{-1}$ is injected into the borehole. The halite concentration at the outer boundary remains at its initial value, which is the equilibrium halite concentration (i.e. $6.217\,mol\,kg^{-1}$) at the working pressure and temperature. This configuration allows the simulation of halite dissolution due to the interaction between the injected fresh water and the rock salt formation. The material properties are presented in Table 1, as obtained from Zill et al.[4] Our simulation fully couples the geochemical reaction (halite dissolution) with the geomechanics.
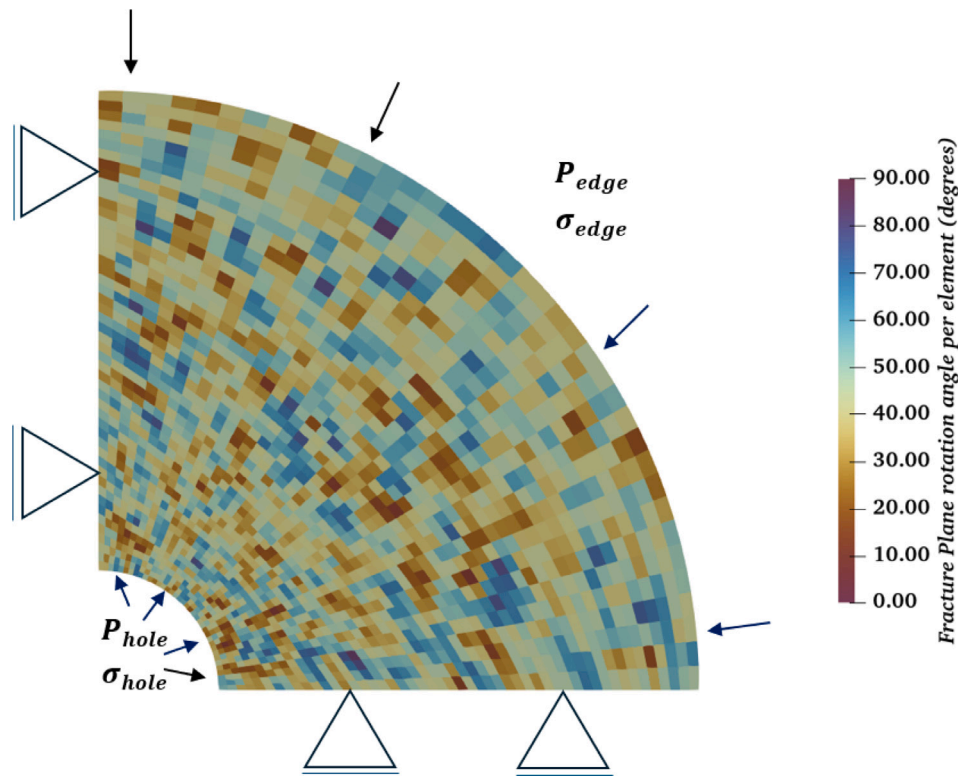
**Fig. 3.** Simulation domain of the cylindrical rock salt volume with the boundary conditions. Here the quasi-isotropic permeability of random fracture rotation.
*Source:* Adapted from Ref. 4.

**Table 1**
Material properties.

| Material property | Symbol | Value | Unit |
|---|---|---|---|
| Fluid density | $\rho_f$ | 1000 | $\mathrm{kg\,m^{-3}}$ |
| Fluid viscosity | $\mu$ | $1.0 \times 10^{-3}$ | Pa s |
| Solid (mineral) density | $\rho_s$ | 2000 | $\mathrm{kg\,m^{-3}}$ |
| Porosity | $\phi_0$ | 0.01 | – |
| Biot's coefficient | $\alpha_B$ | 1.00 | – |
| Intrinsic permeability | $k_m$ | $1.0 \times 10^{-18}$ | $\mathrm{m^2}$ |
| Mean fracture distance | $a$ | $1.0 \times 10^{-2}$ | m |
| Threshold strain | $\varepsilon_0$ | $1.0 \times 10^{-5}$ | – |
| Temperature | $T$ | 327.59 | K |
| Reaction rate constant | $r_+$ | 0.806 354 | $\mathrm{mol\,m^2\,s^2}$ |

Four permeability models were evaluated in the benchmark study by Zill et al.[4] Here we exclude the standard isotropic permeability model from our verification as it is not pertinent to our objective. Instead, we concentrate on the following permeability models: (1) anisotropic permeability, where fracture planes are aligned strictly in the vertical and horizontal directions with no third mutually orthogonal plane due to the 2D scenario; (2) 45° rotation of the fracture planes in the anisotropic permeability model; and (3) quasi-isotropic permeability, achieved by random rotation of fracture normals per element. Fig. 4 shows the results of these three scenarios with HM coupling, including fluid pressure, fluid velocity, and rock salt permeability respectively. Fig. 5 shows the results of the same scenarios considering HMC coupling (with halite dissolution), including the additional field of Na$^+$ concentration.

Figs. 4 and 5 highlight the predictive capability of the proposed permeability model in identifying preferential fluid pathways across the three simulated scenarios. In the anisotropic scenario, fluid flow is primarily directed along the orthogonal fracture planes, as shown by distinct regions of increased fluid pressure, velocity, porosity, and

Na$^+$ concentration corresponding to the horizontal and vertical fracture planes, indicating that both horizontal and vertical fractures are effectively activated.

For the scenario where fracture planes are rotated by 45°, our simulations precisely captures the influences of fracture orientation rotation on fluid pathways. The central images of Fig. 5 display preferential increases in fluid pressure, fluid velocity, permeability and porosity aligned with the 45° orientation. This scenario highlights the model's ability to adapt to rotated fracture sets and emphasizes the importance of considering fracture orientation in predicting fluid pathways.

In the quasi-isotropic scenario, where fracture planes are randomly rotated per element, the model effectively simulates an isotropic-like fluid pressure and permeability distribution. The random orientation of fractures introduces variability in the flow paths, leading to a more dispersed velocity field, as seen in the right images of Fig. 5. Despite this variability, the model still identifies discrete preferential flow paths influenced by localized high-permeability regions, underscoring the impact of fracture orientation randomness on fluid transport.

For all three simulated scenarios, our HMC-coupled permeability model effectively captures the alteration of preferential flow paths due to halite dissolution processes, compared to the HM-coupled permeability model, as illustrated in Fig. 5. The halite dissolution enhances permeability and fluid velocity, leading to higher values in the HMC model compared to the HM-coupled model. Specifically, while the HM model exhibits a similar fluid pressure distribution, it produces a Darcy velocity range of $2.1 \times 10^{-9}\,\mathrm{m\,s^{-1}}$ to $2.2 \times 10^{-6}\,\mathrm{m\,s^{-1}}$, contrasting with a range of $1.3 \times 10^{-8}\,\mathrm{m\,s^{-1}}$ to $1.7 \times 10^{-5}\,\mathrm{m\,s^{-1}}$ in the HMC model. The permeability in the HM model varies from $3.3 \times 10^{-18}\,\mathrm{m^2}$ to $2.7 \times 10^{-14}\,\mathrm{m^2}$, while in the HMC model, it ranges from $1 \times 10^{-18}\,\mathrm{m^2}$ to $2.2 \times 10^{-13}\,\mathrm{m^2}$. This notable increase in permeability, and fluid velocity within the HMC model highlights the critical role of halite dissolution, validating the model's capability to capture complex fluid dynamics and accurately predict enhanced transport properties in reactive systems.
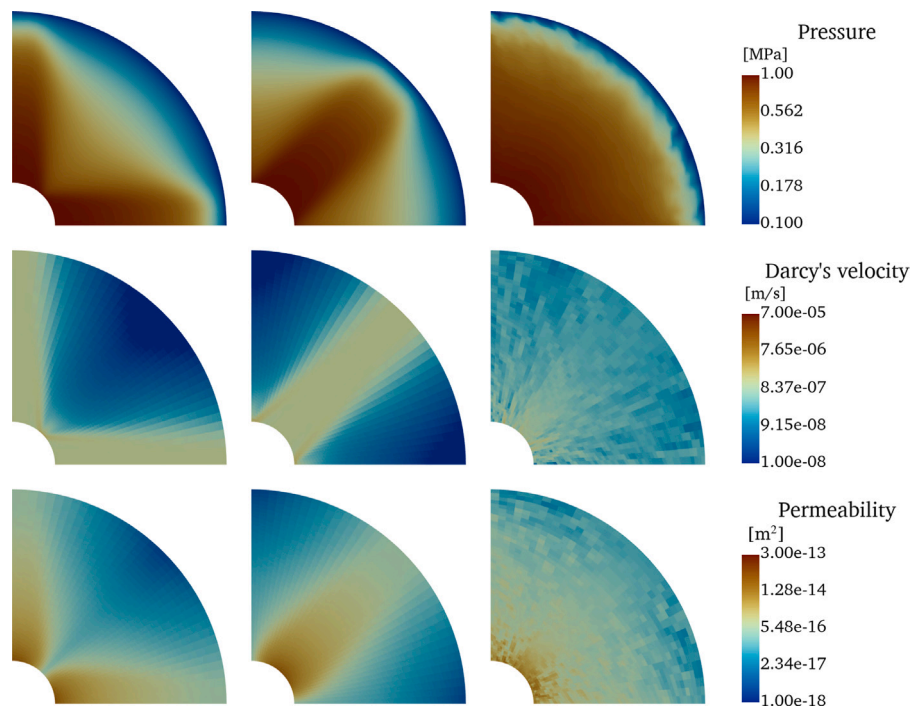
**Fig. 4.** Fluid pressure, Darcy's velocity, and permeability fields for HM coupling (without halite dissolution) shown from left to right for (left) the embedded orthotropic fracture model aligned in both vertical and horizontal directions, (center) the embedded orthotropic fracture model rotated by 45°, and (right) the embedded orthotropic fracture model of randomly-distributed fracture normal.

### 4.2. Application of the proposed HMC model: Effect of geochemical reaction on pressure-driven percolation of fluid through rock salt

To demonstrate the applicability of our extended, HMC-coupled permeability model to real-world scenarios, we use a hydro-frac experiment conducted by Kamlot[30] and numerically verified by Zill et al[4] as a case study. In our simulations, water is injected into the rock salt, and results are compared with the original experimental and numerical studies. The experimental observations show that the injected fluid into rock salt follows preferential paths driven by pressure percolation, which is influenced by the in-situ stress state. A brief overview of the experiment is provided below (for a detailed discussion, see Ref. 4).

#### 4.2.1. Simulation setup: Geometry, material properties and boundary conditions

The benchmark experiment involves injecting fluid through a borehole into rock salt samples kept under constant true triaxial compressive state at room temperature. Kamlot[30] conducted two experiments of different compressive stress states: Experiment 1 was designed to create horizontal flow paths (hydro-frac), while Experiment 2 was aimed at generating vertical flow paths. In both experiments, the injected fluid flows orthogonal to the direction of the minimum principal stress. For this case study, we focus on Experiment 1 (see Fig. 6).

The benchmark experiment employed a cubic rock salt sample with a side length of $10\,\mathrm{cm}$ and a $5\,\mathrm{cm}$ deep borehole drilled into it Ref. 30. The borehole has a diameter of $1.6\,\mathrm{cm}$. The borehole is lined with a hollow steel casing or probe, $0.1\,\mathrm{cm}$ thick, which directs the injected fluid into the rock salt sample through the base of the borehole. The experiment commenced by gradually applying a load to the rock salt sample at a rate of $60\,\mathrm{MPa\,h^{-1}}$, which was then held constant for one hour before fluid injection began. Spindle oil was used as the working fluid. The initial fluid injection rate was set at a low rate of $0.5\,\mathrm{mL\,h^{-1}}$ to ensure that no hydro-frac occurred, allowing the fluid to steadily diffuse into the rock salt, maintaining constant fluid pressure in the borehole. Following this controlled phase, the injection rate was increased to $10\,\mathrm{mL\,h^{-1}}$ to induce hydro-fracturing. Fluid injection was

stopped after the initial breakthrough, marking the formation of the hydro-fracture, and subsequently re-activated to promote the formation of an additional hydro-fracture.

Unlike the original experiment, which used spindle oil, in our simulation we inject "fresh" water into the rock salt to examine the effect of halite geochemical reaction/dissolution on flow paths. Given water's low compressibility, its bulk modulus variations are negligible within the temperature and pressure ranges considered. We use our modified embedded orthotropic fracture permeability model with quasi-isotropy, characterized by random rotation of the three orthotropic fracture planes in each finite element. All relevant material properties used for the simulation can be found in Table 4.

To leverage the problem's symmetry and the quasi-isotropy in the permeability model, we model only a quarter of the sample. As in the referenced numerical study,[4] the bottom edge of the borehole is rounded with a radius of $0.1\,\mathrm{cm}$ to prevent singular fluid pressure points at those sharp edges. To maintain consistency with the numerical benchmark, we assume the casing is made of material with a zero porosity, an extremely low permeability, a Biot's constants of 1.0 [−], and an extremely low Young's modulus, rendering it impermeable to fluid flow.

Our simulation employs a finite element discretization technique similar to the one used in the referenced numerical benchmark,[4] featuring an incremental finite element size that increases with distance from the borehole (see Fig. 7). While the numerical benchmark by Zill et al[4] utilized a mesh with 8304 tetrahedral elements, our simulations achieve faster convergence using a uniform mesh with 656 tetrahedral elements without significant deviation from their benchmark results.

The model volume of the borehole is critical for the stabilization of the injection pressure. Simulating only a quarter section of the borehole is found to result in over-shot pressure in comparison to the experiment. To mitigate this issue, the numerical benchmark adds an extra discretized cube to increase the borehole volume. We take a different approach: our model incorporates the entire borehole rather than a quarter section, ensuring large enough volume and more accurate compliance between the rock salt sample and the injected water.
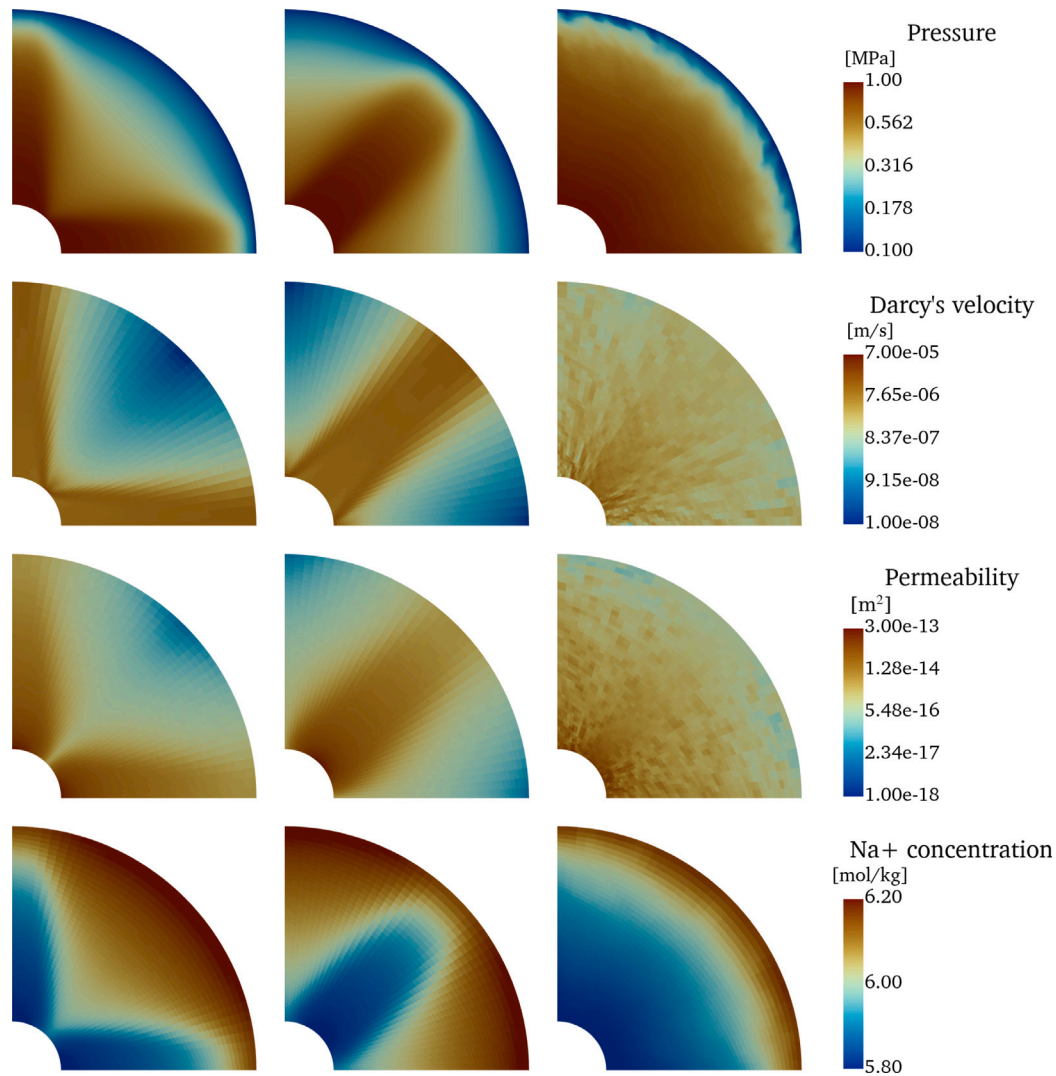
**Fig. 5.** Fluid pressure, Darcy's velocity, permeability, and Na$^+$ concentration fields for HMC coupling (with halite dissolution) shown from left to right for (left) the embedded orthotropic fracture model aligned in both vertical and horizontal directions, (center) the embedded orthotropic fracture model rotated by 45°, and (right) the embedded orthotropic fracture model of randomly-distributed fracture normal.
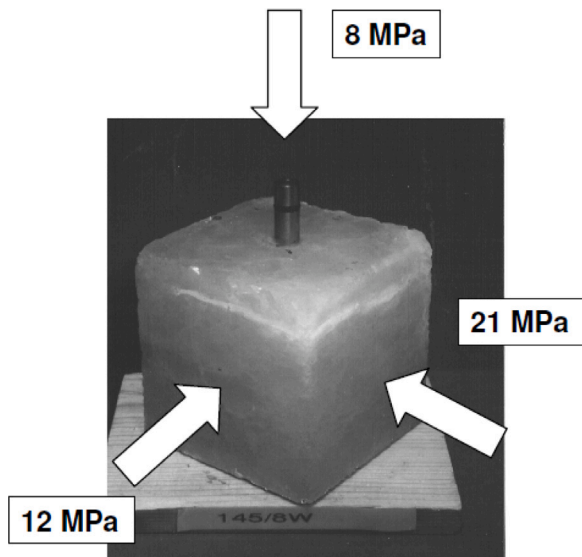


**Fig. 6.** Rock salt sample from Experiment 1 with horizontal fractures and the applied triaxial stress conditions for illustration.[4,30]

Boundary conditions for our model are set as follows. No-flow boundaries and restricted normal displacements are set to the two symmetry faces. Except for the bottom face with the restricted vertical displacement, the other three external faces are subject to mutually orthogonal normal stresses to replicate the triaxial compressive state shown in Fig. 6, with pore pressures assumed to be in equilibrium with atmospheric pressure.

Our simulation begins with initial equilibrium concentrations of Na$^+$ and Cl$^-$ at 25 °C (i.e., 5.45 mol kg$^{-1}$). The injected water has Na$^+$ and Cl$^-$ concentrations of 0 mol kg$^{-1}$, while concentrations of Na$^+$ and Cl$^-$ remain at equilibrium at the outer boundary. We apply the external stress shown in Fig. 6, where $\sigma_1 = 8$ MPa, $\sigma_2 = 12$ MPa, and $\sigma_3 = 21$ MPa. The Newton solver is employed to compute the resulting algebraic equations, using an iterative adaptive time-stepping approach with a nonlinear absolute tolerance of $1 \times 10^{-11}$. The simulation runs for a total modeling time of 40 min (see Tables 2 and 3).

### 4.2.2. Results: HM model

Our first simulation focuses on hydro-mechanical HM coupling without reactive transport. It serves as a numerical case study based on the experimental study by Kamlot[30] and the corresponding numerical simulation by Zill et al.[4] We use the best-fit parameters from the benchmark numerical study (see Table 4) and adopt the same initial injection

**Table 2**
Material properties used to simulate the Kamlot's experiment.[30] Simulation temperature is set at $T = 298.15$ K. The longitudinal dispersivity ($\alpha_L$) and transverse dispersivity ($\alpha_T$) for both $Na^+$ and $Cl^-$ are set to $1.0 \times 10^{-2}$ m and $1.0 \times 10^{-3}$ m, respectively. The borehole chamber has Young's Modulus and Poisson's ratio of 100 GPa and 0.0 to further minimize the deformation of the borehole. The HMC model uses an intrinsic rate constant of $r_+ = 0.616\,595$ mol m$^{-2}$ s$^{-1}$ at the corresponding temperature.

| Material property | Symbol | Domain | Casing | Borehole chamber | Water | Unit |
|---|---|---|---|---|---|---|
| Young's Modulus | $E$ | 25 | 210 | 100 | | GPa |
| Poisson's ratio | $\nu$ | 0.25 | 0.30 | 0.00 | | – |
| Biot's coefficient | $\alpha_B$ | 1.0 | 0.00 | 1.00 | | – |
| Porosity | $\phi$ | 0.01 | 0.00 | 1.00 | | – |
| Intrinsic permeability | $k_m$ | $1 \times 10^{-21}$ | $1 \times 10^{-23}$ | $1 \times 10^{-7}$ | | m$^2$ |
| Solid density | $\rho_s$ | 2000 | 7900 | 2000 | | kg m$^{-3}$ |
| Fluid density | $\rho_f$ | | | | 997 | kg m$^{-3}$ |
| Fluid viscosity | $\mu$ | | | | $0.89 \times 10^{-3}$ | mPa s |
| Fluid bulk modulus | $K$ | | | | 2.2 | GPa |
| Temperature | $T$ | 298.15 | | | | K |
| Reaction rate constant | $r_+$ | 0.616 595 | | | | mol m$^2$ s$^2$ |
| Longitudinal dispersivity | $\alpha_L$ | $1.0 \times 10^{-2}$ | | | | m |
| Transverse dispersivity | $\alpha_T$ | $1.0 \times 10^{-3}$ | | | | m |
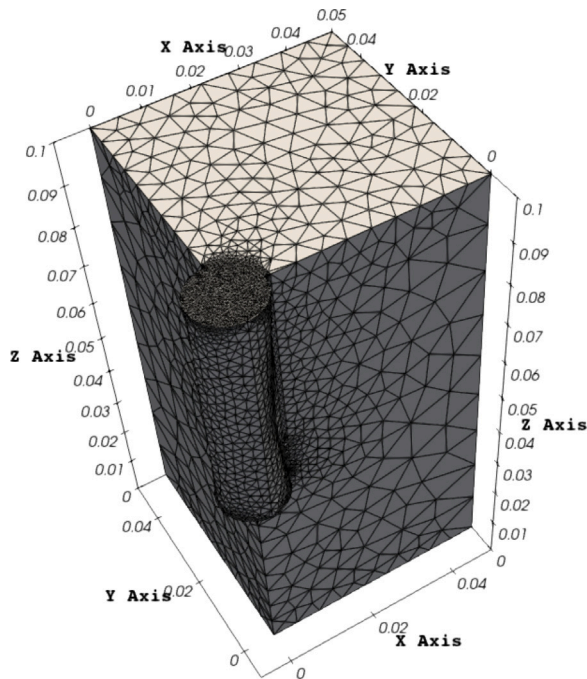


**Fig. 7.** Simulation domain (a quarter section of rock salt) of discretized finite elements.

**Table 3**
Creep parameters for modified Lubby2 creep.
*Source:* Taken from Ref. 60.

| Creep Parameters | Value | Unit |
|---|---|---|
| $G_{K_0}$ | $6.27 \times 10^4$ | MPa |
| $m_g$ | $-0.254$ | MPa$^{-1}$ |
| $\eta_{K_0}$ | $1.66 \times 10^5$ | MPa min |
| $m_2$ | $-0.267$ | MPa$^{-1}$ |
| $\eta_{M_0}$ | $4.03 \times 10^7$ | MPa min |
| $m_1$ | $-0.327$ | MPa$^{-1}$ |
| $\sigma_0$ | 1.0 | MPa |

**Table 4**
Permeability parameters used in the embedded fracture permeability model.

| Material property | Symbol | Value | Unit |
|---|---|---|---|
| Mean fracture distance | $a$ | 0.024 | m |
| Threshold strain | $\varepsilon_0$ | $-3 \times 10^{-5}$ | – |

procedure as in the benchmark simulation: a constant pressure of 1 MPa rather than a volumetric initial injection rate. This procedure ensures that the pressure evolution curves align closely with the experimental results, although it slightly compromises the early rise in fluid pressure.

When the dissolution rate of halite is zero (i.e. no geochemical reactions), our permeability model should effectively replicate the one in the benchmark numerical simulation,[4] serving as a control scenario. This control simulation allowed us to evaluate the model's performance purely under HM coupling, providing a baseline to compare against more complex scenarios involving halite dissolution. Hereafter, the control simulation is called HM coupling model.

Fig. 8 illustrates the pressure and permeability profiles from this HM control simulation, measured at a point (i.e., 0 cm, 0 cm, 0.05 cm) near the injection area within the borehole pressure chamber. The fluid pressure profile, shown on the left of this figure, exhibits the following pattern: initially, constant pore pressure of 1 MPa was observed for approximately 5 min when the fluid injection was low, indicating that fluid was diffusing into the rock salt without inducing hydro-fractures. This constant pressure reflects the initial equilibrium of the fluid pressure before any significant increase in fluid injection. Following this, the pressure rose steadily and remained constant at approximately 8.2 MPa, corresponding to the increased injection rate. The plateau at 8.2 MPa indicates hydro-fracture formation due to the fluid pressure surpassing the minimum principal stress. Upon cessation of fluid injection, the pressure dropped to around 5.5 MPa. After re-injection, the pressure profile increased sharply before stabilizing at 8.2 MPa, indicating another hydro-fracture event.

The permeability profile in Fig. 8 displays a pattern similar to the fluid pressure profile. Initially, during the equilibrium phase with constant fluid pressure at 1 MPa, the permeability remains low and stable at approximately $1.0 \times 10^{-19}$ m$^2$, indicating minimal fluid flowing through the rock salt. As the fluid pressure rises due to the increase in fluid injection rate, the permeability exhibits a sharp increase, reaching a maximum of around $7 \times 10^{-19}$ m$^2$. This sudden rise in permeability suggests the onset of hydro-fracture, enhancing the capacity for fluid flow within the rock salt. When fluid injection ceases after around 19 min, the permeability decreases to approximately $2.0 \times 10^{-17}$ m$^2$, reflecting a reduction in fracture aperture as the system relaxes. Following the resumption of fluid injection at around 30 min, the permeability increases again and stabilizes near $7.0 \times 10^{-19}$ m$^2$, confirming the reactivation and expansion of fractures under renewed pressure conditions. The observed permeability variations closely mirror the pressure fluctuations, underscoring the strong coupling between fluid pressure and permeability in the HM model, particularly during fracture formation and subsequent reactivation events.

The control HM simulation results for fluid pressure and permeability are consistent with experimental observations and the benchmark simulations that used spindle oil as the injection fluid, even though
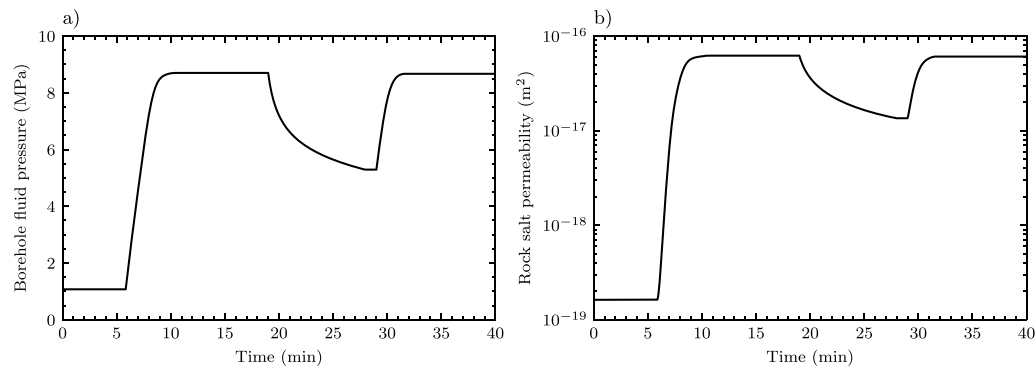
**Fig. 8.** Pressure versus time and permeability versus time profiles from the control HM coupling simulation, demonstrating the fluid pressure evolution and corresponding changes in rock salt permeability during different injection phases.

we used water. This consistency is particularly noteworthy, given that water has a higher density and lower viscosity compared to spindle oil, which typically influences fluid flow dynamics. These results confirm that our permeability model accurately captures the key behaviors observed in the previous studies, validating its effectiveness in replicating the experimental and numerical outcomes.

### 4.2.3. Results: HMC model

The HMC simulation extends the HM model by incorporating halite dissolution effects. As stated in 4.2.1, water of zero concentration of $Na^+$ and $Cl^-$ is injected, using the same injection protocol as in the HM coupling simulation, into the rock salt saturated with equilibrium concentrations of $Na^+$ and $Cl^-$ at 25 °C (i.e., 5.45 mol kg$^{-1}$). The resulting fluid pressure and permeability profiles show a similar pattern to the HM coupling model but with a considerably different magnitudes, emphasizing the influence of halite dissolution on injection.

Fig. 9 illustrates profiles of fluid pressure, permeability, $Cl^-$ concentration, and halite dissolution rate, measured at the same location as in the HM coupling model. Initially, the fluid pressure remains constant at 1 MPa for about 5 min, corresponding to the low injection rate. As the injection rate increases, the pressure rises rapidly, resembling the HM coupling simulation. However, unlike the HM coupling simulation, where the pressure stabilizes at 8.2 MPa, indicating hydro-fracture formation, the HMC coupling simulation yields a much lower stabilized pressure at approximately 5.3 MPa but a slightly quicker increase. After injection ceases, the pressure drops to around 2.5 MPa, much lower than the 5.5 MPa in the HM simulation. Upon re-injection, the fluid pressure rises and stabilizes again at about 5.3 MPa, lower than the 8.2 MPa observed in the HM simulation, highlighting the impact of dissolution on fracture behavior.

The permeability profile in the HMC simulation consistently displays higher magnitudes compared to the HM simulation, except for the period of no injection. During the initial phase, the permeability reaches $4 \times 10^{-18}$ m$^2$, notably higher than the $1 \times 10^{-19}$ m$^2$ observed for the HM simulation. As the injection rate increases, the HMC simulation yields much steeper permeability increase and higher maximum at around $1 \times 10^{-16}$ m$^2$, compared to the HM simulation. Following the injection cessation at around 19 min, the HMC permeability decreases more quickly, reaching a minimum of $1 \times 10^{-17}$ m$^2$, while the HM simulation settles at $2 \times 10^{-17}$ m$^2$. After re-injection at approximately 30 min, the HMC permeability spikes sharply, stabilizing again at $1 \times 10^{-16}$ m$^2$. The permeability observations suggest that halite dissolution in the HMC model enhances fluid pathways, leading to more rapid permeability increases and greater sensitivity to injection rates than in the HM simulation. The $Cl^-$ concentration initially remains steady at 5.45 mol kg$^{-1}$ during the low injection phase. As the injection rate increases, the concentration decreases slightly to approximately 5.42 mol kg$^{-1}$ due to the flushing of fresh water. After the cessation

of injection, the $Cl^-$ concentration steadily rises to 5.42 mol kg$^{-1}$ before gradually decreasing to approximately 5.41 mol kg$^{-1}$ following re-injection. These observations indicate that the halite dissolution process is regulated by fluid injection, with lower concentrations reflecting enhanced flushing by fresh water. The slight concentration increase after injection stops suggests a re-equilibration of the system as dissolution slows down.

The dissolution rate profile initially shows a steady value of 0.001 mol m$^{-2}$ s$^{-1}$ during the low injection phase. As the injection rate increases, the dissolution rate surges sharply to approximately 0.005 mol m$^{-2}$ s$^{-1}$. Once the injection stops, the dissolution rate decreases quickly to about 0.0015 mol m$^{-2}$ s$^{-1}$. Upon re-injection, the dissolution rate sharply increases to approximately 0.006 mol m$^{-2}$ s$^{-1}$. The dissolution rate behavior reflects a direct correlation with fluid injection. The observed dissolution rate and $Cl^-$ concentration behaviors indicate that halite dissolution, driven by fluid injection, enlarges the fracture aperture, which in turn increases permeability.

## 5. Discussion

The HMC coupling model developed in this study explores the effect of halite dissolution in rock salt formations undergoing PDP (pressure-driven percolation) due to water injection. This section investigates how halite dissolution in the HMC simulation influences the pressure and permeability evolution compared to those in the HM simulation.

Our HMC simulation indicates that halite dissolution plays a critical role in enhancing permeability by creating additional pathways and increasing the overall capacity for fluid flow within rock salt formations. In the HMC simulation, the dissolution process erodes grain boundaries and enlarges existing pores, allowing fluid to percolate through a more expansive network of fractures. This expanded fracture network reduces the resistance to fluid flow, requiring less pressure gradient to achieve the same volumetric injection rate. Consequently, the fluid pressure in the HMC simulation stabilizes at a lower value, around 5.3 MPa, compared to 8.2 MPa in the HM simulation. The enhanced permeability accelerates the system's response to fluid injection, enabling faster stabilization of fluid flow. The lower pressure required to maintain the same volumetric rate is a direct result of the increased permeability, confirming that chemical processes such as halite dissolution significantly impact the mechanical behavior of the system. This demonstrates that reactive transport, in conjunction with hydro-mechanical processes, must be considered for accurate predictions in fluid injection scenarios.

Although our current HMC model does not account for it, the dissolution of grain boundaries, in reality, can weaken the mechanical strength of rock salt. This weakening reduces the stiffness of the formation, making it more prone to hydro-fracturing. As a result, the fluid pressure required to initiate fractures could decrease, which might be advantageous for geothermal systems that rely on consistent fluid flow
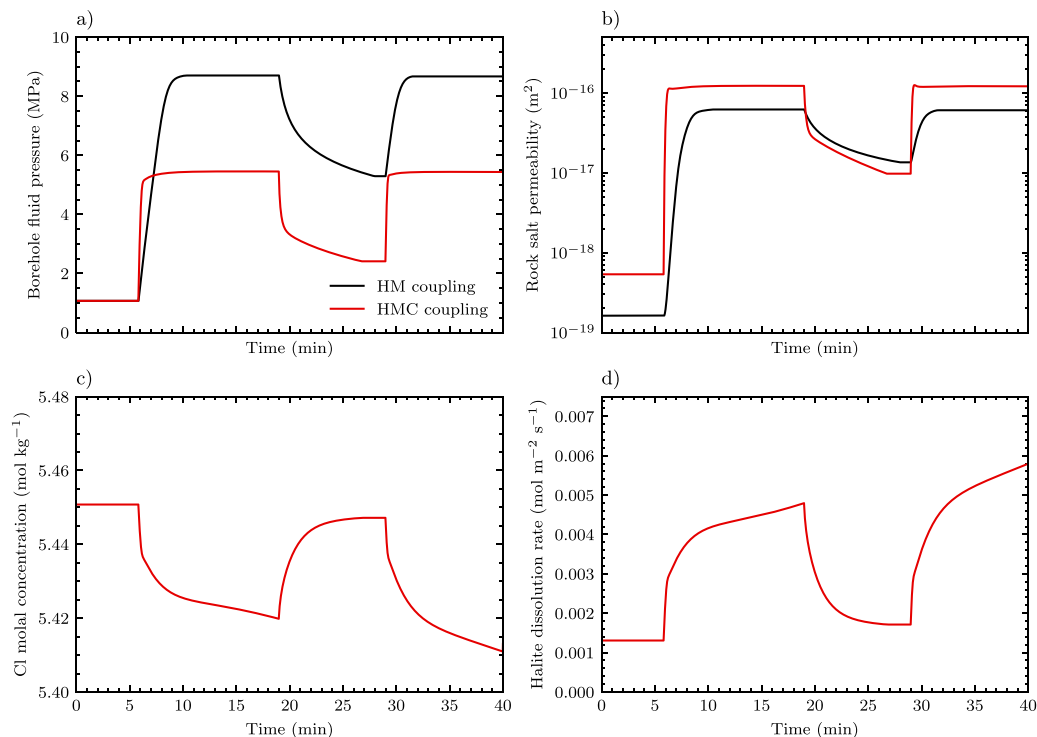
**Fig. 9.** Comparison of fluid pressure (a) and permeability (b) between the HM and HMC models, and the corresponding Cl⁻ concentration (c) and halite dissolution rate (d).

without the need for high injection pressures. On the other hand, this characteristic could be problematic in cases where rock salt formations serve as hydraulic barriers, as it may compromise their ability to effectively contain or restrict fluid movement.

In this study, we considered rock salt to deform elastically only, due to the laboratory scale nature of the numerical scenarios we covered. Over larger timescales — ranging from the operational timescale of subsurface energy storage to geological timescale — rock salt deforms in a time-dependent manner with a viscoplastic behavior accompanied by damage when the applied stresses exceed its dilatancy limit.[57] These mechanisms are important to capture as they will dominate the deformation of rock salt formations and therefore control the geomechanical stability and sustainability of subsurface energy operations targeting those formations.[63] This is particularly relevant in the case of seasonal energy or hydrogen storage in salt caverns where the rock salt will be subject to cycling mechanical loading which can induce tensile cracking in the cavern walls. Future work should therefore investigate the macroscale impact of these deformation mechanisms on the mechanical integrity of subsurface energy infrastructure and on the deformation-induced permeability increase in rock salt.

## 6. Conclusion

This study proposes an HMC model for simulating pressure-driven percolation[2,4] or pressure-driven infiltration[9,10,12,13] in rock salt formations. To capture this behavior efficiently, we modified the deformation-dependent permeability model developed by Zill et al[4] to account for the possible influence of geochemical reactions (i.e., halite dissolution) occurring in the rock salt due to fluid injection.

The fully coupled, fully implicit reactive transport model adopted in this study contained a geochemical reaction/dissolution rate based on the Transition State Theory (TST)[33] and following the methodology

outlined by Seales et al.[32] To verify our model, we reference experimental work from Kamlot,[30] which was numerically validated by Zill et al.[4]

The results of our HMC models confirms the significant role of geochemical reactions in rock salt formations undergoing pressure-driven percolation due to fluid (water) injection. The dissolution reactions notably contribute to the reduction of pore pressure in the formations, making them crucial for practical considerations. While our model provides valuable initial insights, it also highlights the necessity for more advanced and comprehensive modeling approaches in future studies.

Future models should improve the representation of rock salt geomechanical behavior by incorporating mechanisms such as damage and healing, particularly for induced stresses that exceed the dilatancy limit. Additionally, thorough experimental studies are required to validate the numerical model. Upscaling fractures in permeability models, such as the one proposed here, presents significant challenges, especially for large-scale applications and over extended timeframes. Therefore, careful consideration of fracture parameters is crucial for accurate large-scale simulations. For instance, fracture geometry and aperture distribution have a significant impact on permeability, while the density and distribution of fractures influence connectivity and fluid flow dynamics. Efficient calibration of these parameters with field test data is essential to enhance model accuracy. Moreover, validating simulation results against field-scale tests is critical to ensure confidence in the model's parameters and its application to real-world scenarios involving rock salt geological formations. Addressing these factors is key to making the model reliable for practical use.

Nevertheless, this work establishes a numerical framework for advancing the predictive capabilities of coupled hydro-mechanical–chemical processes in rock salt formations. It improves our understanding of reactive transport dynamics within these geological systems, providing valuable insights for future research and practical applications.
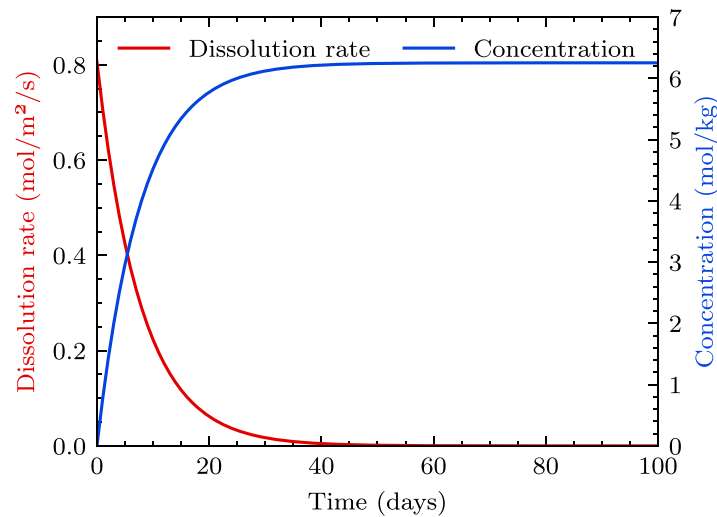
**Fig. A.10.** A graph of halite dissolution rate and species concentration versus time.

## CRediT authorship contribution statement

**Ishmael Dominic Yevugah:** Writing – review & editing, Writing – original draft, Software, Methodology, Conceptualization. **Xiang-Zhao Kong:** Writing – review & editing, Validation, Supervision, Conceptualization. **Antoine B. Jacquey:** Writing – review & editing, Validation, Software. **Christopher P. Green:** Validation, Software. **Hartmut M. Holländer:** Writing – review & editing, Supervision, Funding acquisition. **Pooneh Maghoul:** Writing – review & editing, Supervision, Funding acquisition.

## Code and data availability

The code used for this research is available online (open-source) and appropriately cited in the manuscript. https://github.com/idaholab/moose.

## Declaration of competing interest

The authors declare that they have no known competing financial interests or personal relationships that could have appeared to influence the work reported in this paper.

## Acknowledgment

## Appendix. Verification test: Halite dissolution kinetics

The verification test for the implemented halite dissolution rate model follows the numerical simulation conducted by Seales et al[32] to describe halite dissolution in the Marcellus shale formation during hydraulic fracturing. Replicating this numerical simulation and comparing our results ensured quality control of the chemical component of our proposed HMC model. With this, the following assumptions propounded below hold for their numerical simulation.

The dissolution of halite mineral occurs in a $1.0\,L$ aqueous fluid (water) following the reaction rate described by Eq. (10), assuming an isothermal condition of $327.594\,K$. At this temperature, the equilibrium concentration of halite is $6.217\,mol\,L^{-1}$ ($\sim 363.347\,g\,L^{-1}$) according to Seales et al.[32] Taking into account the density of water ($1\,kg\,L^{-1}$), the molality of halite at this saturation temperature corresponds to

$\frac{6.217\,mol\,L^{-1}}{1\,kg\,L^{-1}} = 6.217\,mol\,kg^{-1}$, which gives an equilibrium constant ($k_{eq}$) of $38.65\,mol^2\,kg^{-2}$. Our simulation started at $1\,mol\,kg^{-1}$ of halite with an extremely low concentration of Na$^+$ and Cl$^-$ (i.e., $1 \times 10^{-8}\,mol\,kg^{-1}$), far from equilibrium and ended at the equilibrium concentration of the chemical species (i.e., $6.217\,mol\,kg^{-1}$).

Other pertinent assumptions are as follows: a unit reactive surface area, a neutral pH, a Temkin's average coefficient equal to $2$[44] to fit our numerical results, and an intrinsic rate constant of $0.806\,354\,mol\,m^{-2}\,s^{-1}$ corresponding to a temperature of $327.59\,K$ ($\sim 54.44\,^\circ C$) obtained via the Arrhenius phenomenological law. The simulation also assumes that the primary species (i.e., Na$^+$ and Cl$^-$) have no preferential detachment from the halite mineral surface. Based on these assumptions, the simulation proceeds for $2160\,h$ ($90\,d$) with a Newton solution to the resulting algebraic equations at an iterative adaptive time step size of $1 \times 10^{-2}$ and a nonlinear absolute tolerance of $1 \times 10^{-10}$. Fig. A.10 shows the result of our simulation.

As expected, our numerical model correctly predicted the equilibrium concentration of the chemical species ($6.217\,mol\,kg^{-1}$) starting from the initially low concentration. Also, the halite mineral dissolves reasonably to equilibrium. Thus, based on the TST theory and Pitzer's specific ion interaction theory (SIT), our model can simulate halite dissolution up to higher ionic strengths ($20$ molal) and is therefore used in this study.

## Data availability

The code used for this research is available online (open-source) and appropriately cited in the manuscript. https://github.com/idaholab/moose.

## References

1. Hunsche U, Hampel A. Rock salt—the mechanical properties of the host rock material for a radioactive waste repository. *Eng Geol.* 1999;52(3–4):271–291.
2. Lüdeling C, Naumann D, Minkley W. Investigation of fluid transport in rock salt under repository-relevant conditions–the PeTroS project. In: *The Mechanical Behavior of Salt X: Proceedings of the 10th Conference on the Mechanical Behavior of Salt (SaltMech x), Utrecht, the Netherlands, 06-08 July 2022.* CRC Press; 2022:200.
3. Tounsi H, Rutqvist J, Hu M, Wolters R. Numerical investigation of heating and cooling-induced damage and brine migration in geologic rock salt: Insights from coupled THM modeling of a controlled block scale experiment. *Comput Geotech.* 2023;154:105161.
4. Zill F, Lüdeling C, Kolditz O, Nagel T. Hydro-mechanical continuum modelling of fluid percolation through rock salt. *Int J Rock Mech Min Sci.* 2021;147:104879.
5. Jackson MP, Hudec MR. *Salt Tectonics: Principles and Practice.* Cambridge University Press; 2017.

6. Watanabe T, Peach CJ. Electrical impedance measurement of plastically deforming halite rocks at 125 C and 50 MPa. *J Geophys Res Solid Earth*. 2002;107(B1):ECV–2.

7. Popp T, Kern H, Schulze O. Evolution of dilatancy and permeability in rock salt during hydrostatic compaction and triaxial deformation. *J Geophys Res Solid Earth*. 2001;106(B3):4061–4078.

8. Schulze O, Popp T, Kern H. Development of damage and permeability in deforming rock salt. *Eng Geol*. 2001;61(2–3):163–180.

9. Wolters R, Lux K, Düsterloh U, et al Evaluation of rock salt barriers with respect to tightness: influence of thermomechanical damage, fluid infiltration and sealing/healing. In: *Proceedings of the Seventh International. Conference on the Mechanical Behavior of Salt (SaltMech7), Paris, 16-19 April 2012*. 2012:425–434.

10. Blanco-Martín L, Wolters R, Rutqvist J, Lux K-H, Birkholzer JT. Thermal–hydraulic–mechanical modeling of a large-scale heater test to investigate rock salt and crushed salt behavior under repository conditions for heat-generating nuclear waste. *Comput Geotech*. 2016;77:120–133.

11. Minkley W, Knauth M, Wüste U. Integrity of salinar barriers under consideration of discontinuum-mechanical aspects. In: *Mechanical Behaviour of Salt VII*. CRC Press; 2012:483–492.

12. Martín LB, Wolters R, Rutqvist J, Lux K-H, Birkholzer JT. Comparison of two simulators to investigate thermal–hydraulic–mechanical processes related to nuclear waste isolation in saliferous formations. *Comput Geotech*. 2015;66:219–229.

13. Blanco-Martín L, Rutqvist J, Battistelli A, Birkholzer JT. Coupled processes modeling in rock salt and crushed salt including halite solubility constraints: Application to disposal of heat-generating nuclear waste. *Transp Porous Media*. 2018;124:159–182.

14. Hou Z. Mechanical and hydraulic behavior of rock salt in the excavation disturbed zone around underground facilities. *Int J Rock Mech Min Sci*. 2003;40(5):725–738.

15. Rouabhi A, Hévin G, Soubeyran A, Labaune P, Louvet F. A multiphase multicomponent modeling approach of underground salt cavern storage. *Geomech Energy Environ*. 2017;12:21–35.

16. Lüdeling C, Minkley W, Naumann D. Pressure-driven percolation in rock salt and barrier integrity in the high-pT regime—the PeTroS project. In: *Geophysical Research Abstracts*. 2019. vol. 21.

17. Sobolik SR, Vignes C, Buchholz S, Keffeler E, Reedlunn B. WEIMOS: Shear behaviors of bedded salt clay seams and their impact on disposal room porosity. In: *The Mechanical Behavior of Salt X*. CRC Press; 2022:168–179.

18. Lewis S, Holness M. Equilibrium halite-H2O dihedral angles: High rock-salt permeability in the shallow crust? *Geology*. 1996;24(5):431–434.

19. Ghanbarzadeh S, Hesse MA, Prodanović M, Gardner JE. Deformation-assisted fluid percolation in rock salt. *Science*. 2015;350(6264):1069–1072.

20. Urai J, Schléder Z, Spiers C, Kukla P. Flow and transport properties of salt rocks. In: *Dynamics of Complex Intracontinental Basins: the Central European Basin System*. Springer Berlin; 2008:277–290.

21. Goodwin N, Graham GM, Frigo DM, Kremer E. Halite deposition–prediction and laboratory evaluation. In: *SPE International Oilfield Scale Conference and Exhibition?* SPE; 2016:SPE–179861.

22. Ranganathan V, Hanor JS. Density-driven groundwater flow near salt domes. *Chem Geol*. 1988;74(1–2):173–188.

23. Zidane A, Zechner E, Huggenberger P, Younes A. Simulation of rock salt dissolution and its impact on land subsidence.. *Hydrol Earth Syst Sci Discuss*. 2013;10(10).

24. Zechner E, Konz M, Younes A, Huggenberger P. Effects of tectonic structures, salt solution mining, and density-driven groundwater hydraulics on evaporite dissolution (Switzerland). *Hydrogeol J*. 2011;19(7):1323–1334.

25. Lisjak A, Grasselli G. A review of discrete modeling techniques for fracturing processes in discontinuous rock masses. *J Rock Mech Geotech Eng*. 2014;6(4):301–314.

26. Lisjak A, Tatone BS, Mahabadi OK, Grasselli G, Marschall P, Lanyon GW, Vaissière Rdl, Shao H, Leung H, Nussbaum C. Hybrid finite-discrete element simulation of the EDZ formation and mechanical sealing process around a microtunnel in Opalinus Clay. *Rock Mech Rock Eng*. 2016;49:1849–1873.

27. Müller C, Frühwirt T, Haase D, Schlegel R, Konietzky H. Modeling deformation and damage of rock salt using the discrete element method. *Int J Rock Mech Min Sci*. 2018;103:230–241.

28. Feng K, Li W, Nan X, Yang G. Salt cavern thermal damage evolution investigation based on a hybrid continuum-discrete coupled modeling. *Sustainability*. 2023;15(11):8718.

29. Alonso E, Olivella S, Arnedo D. Mechanisms of gas transport in clay barriers. *J Iberian Geol*. 2006;32(2):175–196.

30. Kamlot W-P. *Gebirgsmechanische Bewertung der Geologischen Barrierefunktion des Hauptanhydrits in Einem Salzbergwerk* [Ph.D. thesis]. Zugl.: Freiberg (Sachsen), Techn. Univ., Habil.-Schr., 2009; 2009.

31. Grimm Lima M, Schädle P, Green CP, Vogler D, Saar MO, Kong X-Z. Permeability impairment and salt precipitation patterns during CO 2 injection into single natural brine-filled fractures. *Water Resour Res*. 2020;56(8):e2020WR027213.

32. Seales M, Dilmore RM, Ertekin T, Wang JY. Development of a halite dissolution numerical model for hydraulically fractured shale formations (Part I). *J Unconv Oil Gas Resour*. 2016;15:66–78.

33. Lasaga AC. Transition state theory. *Rev Mineral (US)*. 1981;8.

34. Laouafa F, Guo J, Quintard M. Underground rock dissolution and geomechanical issues. *Rock Mech Rock Eng*. 2021;54(7):3423–3445.

35. Permann CJ, Gaston DR, Andrš D, Carlsen RW, Kong F, Lindsay AD, Miller JM, Peterson JW, Slaughter AE, Stogner RH, et al MOOSE: Enabling massively parallel multiphysics simulation. *SoftwareX*. 2020;11:100430.

36. Zhang D, Skoczylas F, Agostini F, Jeannin L. Experimental investigation of gas transfer properties and stress coupling effects of salt rocks. *Rock Mech Rock Eng*. 2020;53:4015–4029.

37. Wilkins A, Green CP, Ennis-King J. An open-source multiphysics simulation code for coupled problems in porous media. *Comput Geosci*. 2021;154:104820.

38. Xie M, Kolditz O, Moog HC. A geochemical transport model for thermo-hydro-chemical (THC) coupled processes with saline water. *Water Resour Res*. 2011;47(2).

39. Gelhar LW, Welty C, Rehfeldt KR. A critical review of data on field-scale dispersion in aquifers. *Water Resour Res*. 1992;28(7):1955–1974.

40. Lichtner PC. Continuum formulation of multicomponent-multiphase reactive transport. *Rev Miner*. 1996;34:1–82.

41. Steefel CI, DePaolo DJ, Lichtner PC. Reactive transport modeling: An essential tool and a new research approach for the earth sciences. *Earth Planet Sci Lett*. 2005;240(3–4):539–558.

42. Guimarães LdN, Gens A, Olivella S. Coupled thermo-hydro-mechanical and chemical analysis of expansive clay subjected to heating and hydration. *Transp Porous Media*. 2007;66:341–372.

43. Carrera J, Saaltink MW, Soler-Sagarra J, Wang J, Valhondo C. Reactive transport: a review of basic concepts with emphasis on biochemical processes. *Energies*. 2022;15(3):925.

44. Crundwell FK. Path from reaction control to equilibrium constraint for dissolution reactions. *ACS Omega*. 2017;2(8):4845–4858.

45. Bethke CM. *Geochemical and Biogeochemical Reaction Modeling*. Cambridge University Press; 2022.

46. Alkattan M, Oelkers EH, Dandurand J-L, Schott J. Experimental studies of halite dissolution kinetics, 1 the effect of saturation state and the presence of trace metals. *Chem Geol*. 1997;137(3–4):201–219.

47. Laidler KJ. The development of the arrhenius equation. *J Chem Educ*. 1984;61(6):494.

48. Pitzer KS. Thermodynamics of electrolytes. V. Effects of higher-order electrostatic terms. *J Solut Chem*. 1975;4:249–265.

49. Baes CF, Mesmer RE. The hydrolysis of cations. 1976 (No Title).

50. Bethke CM. Geochemist's workbench. 1995.

51. Wolery TJ. *EQ3/6, a Software Package for Geochemical Modeling of Aqueous Systems: Package Overview and Installation Guide (Version 7.0)*. Technical Report; Lawrence Livermore National Lab.; 1992.

52. Helgeson HC, Kirkham DH. Theoretical prediction of the thermodynamic behavior of aqueous electrolytes at high pressures and temperatures; II, Debye–Huckel parameters for activity coefficients and relative partial molal properties. *Am J Sci*. 1974;274(10):1199–1261.

53. Malmberg C, Maryott A. Dielectric constant of water from 0 to 100 c. *J Res Natl Bur Stand*. 1956;56(1):1–8.

54. Biot MA. General theory of three-dimensional consolidation. *J Appl Phys*. 1941;12(2):155–164.

55. Bear J. Dynamics of fluids in porous media. *Soil Sci*. 1975;120(2):162–163.

56. Coussy O. *Poromechanics*. John Wiley & Sons; 2004.

57. Cristescu N. Time effects in rock mechanics. In: *Proceedings of the SME Annual Conference, Albuquerque, New Mexico*. Citeseer; 2009:1–4.

58. Zhu C, Arson C. A model of damage and healing coupling halite thermo-mechanical behavior to microstructure evolution. *Geotech Geol Eng*. 2015;33:389–410.

59. Nagel T, Minkley W, Böttcher N, Naumov D, Görke U-J, Kolditz O. Implicit numerical integration and consistent linearization of inelastic constitutive models of rock salt. *Comput Struct*. 2017;182:87–103.

60. Zhang N, Nagel T. Error-controlled implicit time integration of elasto-viscoplastic constitutive models for rock salt. *Int J Numer Anal Methods Geomech*. 2020;44(8):1109–1127.

61. Oron AP, Berkowitz B. Flow in rock fractures: The local cubic law assumption reexamined. *Water Resour Res*. 1998;34(11):2811–2825.

62. Knauth M. Diskontinuumsmechanische modellierung von salzgesteinen. 2018.

63. Ramesh Kumar K, Honorio H, Chandra D, Lesueur M, Hajibeygi H. Comprehensive review of geomechanics of underground hydrogen storage in depleted reservoirs and salt caverns. *J Energy Storage*. 2023;73:108912. http://dx.doi.org/10.1016/j.est.2023.108912,